AFRL-AFOSR-JP-TR-2022-0045

Bio-integrated sensor patch comprising semiconducting silicon nanoneedles for intratissue and intracellular recording

Lee, Chi Hwan
PURDUE UNIVERSITY
2550 NORTHWESTERN AVE STE 1900
WEST LAFAYETTE, IN, 47906
USA

06/02/2022
Final Technical Report

Air Force Research Laboratory
Air Force Office of Scientific Research
Asian Office of Aerospace Research and Development
Unit 45002, APO AP 96338-5002

REPORT DOCUMENTATION PAGE

PLEASE DO NOT RETURN YOUR FORM TO THE ABOVE ORGANIZATION.

1. REPORT DATE	2. REPORT TYPE	3. DATES COVERED	
20220602	Final	START DATE 20180803	END DATE 20220402

4. TITLE AND SUBTITLE
Bio-integrated sensor patch comprising semiconducting silicon nanoneedles for intratissue and intracellular recording

5a. CONTRACT NUMBER	5b. GRANT NUMBER	5c. PROGRAM ELEMENT NUMBER
	FA2386-18-1-4071	
5d. PROJECT NUMBER	**5e. TASK NUMBER**	**5f. WORK UNIT NUMBER**

6. AUTHOR(S)
Chi Hwan Lee

7. PERFORMING ORGANIZATION NAME(S) AND ADDRESS(ES)	8. PERFORMING ORGANIZATION REPORT NUMBER
PURDUE UNIVERSITY 2550 NORTHWESTERN AVE STE 1900 WEST LAFAYETTE, IN 47906 USA	

9. SPONSORING/MONITORING AGENCY NAME(S) AND ADDRESS(ES)	10. SPONSOR/MONITOR'S ACRONYM(S)	11. SPONSOR/MONITOR'S REPORT NUMBER(S)
AOARD UNIT 45002 APO AP 96338-5002	AFRL/AFOSR IOA	AFRL-AFOSR-JP-TR-2022-0045

12. DISTRIBUTION/AVAILABILITY STATEMENT
A Distribution Unlimited: PB Public Release

13. SUPPLEMENTARY NOTES

14. ABSTRACT
The ability to efficiently record or transfer information from/to biological systems such as cells and tissues is limited by which current techniques suffer from the low temporal and spatial resolutions. This collaborative research aims to develop a mechanically flexible and
elastic sensor patch that is capable of intimately interfacing with the curvilinear surface of biological systems in a minimally invasive manner. Uniquely, the sensor patch will include a vertically ordered array of semiconducting Si nanoneedles (Si NNs) to serve as the active sensing element that can measure high-level of electrophysiological signals at the nanoscale. The expected outcome will provide a first-of-its-kind mechanically compliant nanoprobe based on a vertically ordered array of Si NNs for efficient intracellular and intratissue
recordings. The functionalities of the proposed nanoprobe platform can be potentially extendable to many other applications such as nanoscale electrical stimulations, on-demand localized drug deliveries, and optogenetic light-emitting diodes by modulating the embedded electronic properties and/or compositions of the nanoneedles.

15. SUBJECT TERMS

16. SECURITY CLASSIFICATION OF:			17. LIMITATION OF ABSTRACT	18. NUMBER OF PAGES
a. REPORT	b. ABSTRACT	c. THIS PAGE		
U	U	U	SAR	47

19a. NAME OF RESPONSIBLE PERSON	19b. PHONE NUMBER *(Include area code)*
TONY KIM	315-227-7008

PROJECT TITLE

Bio-integrated Sensor Patch Comprising Semiconducting Silicon Nanoneedles for Intratissue and Intracellular Recording

ABSTRACT

Conventional melanoma therapies suffer from the toxicity and side effects of repeated treatments due to the aggressive and recurrent nature of melanoma cells. Less-invasive topical chemotherapies by utilizing microneedles are emerged as an alternative, but the sustained, long-lasting release of drug cargos remains challenged. In addition, the size of the microneedles is relatively large for small, curvilinear, or/and sensitive regions of tissues such as cornea (for ocular melanoma). Here, we report a design of bioresorbable, miniaturized porous-silicon (p-Si) nanoneedles with covalently linked drug cargos at doses comparable to those of microneedles, which is all built on a water-soluble medical film. The water-soluble film serves as a temporary holder that can be flexibly interfaced with the curvilinear surface of living tissues during the insertion of the p-Si nanoneedles, followed by rapid, complete dissolution within one minute. Consequently, the p-Si nanoneedles remain embedded inside tissues and subsequently undergo gradual dissolution allowing for sustained release of the drug cargos. Its utility in unobtrusive topical delivery of chemotherapy with minimal side effects is demonstrated in a murine melanoma model.

INTRODUCTION

Melanoma – the most serious form of skin cancer – is typically caused by ultraviolet radiation from natural sunshine or tanning beds and developed at the stratum corneum of epidermis

(15-25 μm from the skin surface).[1,2] Given the aggressive and recurrent nature of melanoma cells, repeated treatments are often necessary, thereby increasing the risk of toxicity and side effects.[3] An effective treatment involves topical administration of chemotherapeutics into tumor tissues using polymeric microneedles, providing a less-invasive and painless route.[4-12] Recently, further miniaturized nanoscale needles made of porous-silicon (p-Si) emerge as an attractive candidate for intratissue injection that can offer favorable safety profile and controlled biodegradability.[13-16] Unlike conventional polymeric microneedles, the inorganic p-Si nanoneedles greatly benefit from their amenability to existing nanofabrication processing, allowing for (1) precise control of the size, geometry, tapering, and tip morphology at the nanoscale,[17,18] (2) rational tuning of porosity on the surface (in turn, drug loading capacity),[14,19] (3) pre-programmable dissolution rate of p-Si nanoneedles through surface oxidations (encapsulation),[20.21] (4) uniform delivery owing to the high density of p-Si nanoneedles per projected surface area,[13] and (5) long-lasting release of covalently linked drug cargos by gradual degradation of p-Si nanoneedles in tissue fluids over time.[22,23] These attributes are important for controlled, sustained, and minimally invasive topical delivery of therapeutics.

However, challenges still remain in that the vertical array of p-Si nanoneedles need to be built on a Si wafer to accommodate the conditions required for conventional nanofabrication processing such as thermal annealing, corrosive chemical etching, or/and lithographic patterning.[24,25] The use of the rigid, flat Si wafer results in a large mechanical mismatch when interfaced with the soft, curvilinear, and dynamic surface of living tissues. This discordance leads to debasing of the interfacial contact quality, which is particularly problematic in applications to small, curvilinear or/and sensitive regions of tissues such as cornea where melanoma is occasionally formed (i.e., ocular melanomas).[26] A recent work demonstrates that these challenges

can be alleviated to some extent by building the p-Si nanoneedles on a thin, flexible backing film made of silicone elastomer such as polydimethylsiloxane (PDMS).[27] A disadvantage of this construct is that the flexible backing film could cause irritation to the wearer especially under vigorous deformations of tissues by body movements, or otherwise could be partly delaminated from the surface. Complete elimination of the backing film after the insertion of the p-Si nanoneedles into tissues may resolve the physical strains, thereby enabling unobtrusive topical delivery of therapeutics over a prolonged period of time.

Here, we introduce a precisely engineered bioresorbable nanoneedles that comprises of a vertically ordered array of bioresorbable p-Si nanoneedles with covalently linked drug cargos, all of which is built on a thin, flexible, and water-soluble medical film. The water-soluble film is temporarily used during the insertion of the p-Si nanoneedles into tissues, and then can be immediately dissolved within one minute by the application of saline. Consequently, the p-Si nanoneedles remain embedded inside tissues and, due to the nanoscale size, become unobtrusive (nearly unnoticeable) to the wearer without affecting natural motions. The p-Si nanoneedles subsequently undergo gradual hydrolysis in tissue fluids to degrade into biocompatible byproducts, leading to sustained, long-lasting release of preloaded drug cargos over days at a controlled rate. Comprehensive experimental and computational studies provide an insight into the structural design and construction of the p-Si nanoneedles on a water-soluble backing over centimeter-scale areas and elucidate the fundamental attributes. Comprehensive demonstrations of the p-Si nanoneedles for the unobtrusive topical delivery of chemotherapy in a murine melanoma model in vitro, ex vivo, and in vivo illustrate the utility of this concept.

KEY RESULTS AND DISCUSSION

The Design principle and fabrication process

Figure 1A schematically illustrates the basic procedure to integrate vertically ordered p-Si nanoneedles with a thin, flexible, and water-soluble medical film such as polyvinyl alcohol (PVA; medical-grade, molecular weight = ~31,000, Sigma Aldrich, USA). The first step is to fabricate an array of vertical p-Si nanoneedles on a polished monocrystalline Si wafer through sequential steps of photolithographic patterning, dry and wet etchings, and metal-assisted chemical etching (MACE),[27] by which controlled undercuts and nanopores are formed at the bottom and on the surface of the p-Si nanoneedles, respectively (Figure 1A, left). Details of the fabrication procedures are shown in Methods section. Figure S1 shows representative scanning electron microscopy (SEM) images of the as-fabricated p-Si nanoneedles, exhibiting the tip diameter (d) of 150 nm-2 μm, the base diameter (D) of 2-4 μm, and the length (L) of 10-70 μm. In the next step, the entire structure is spin-cast with a solution of 10 weight % PVA, allowing an air gap to form at the interface due to surface tension (Figure 1A, middle). The air gap is to determine the length of the p-Si nanoneedles, which can be controlled by adjusting the spin-casting speed (in rpm) and, if necessary, repeating the casting cycles. A subsequent thermal annealing in a convection oven at 70°C for 30 min completes the solidification of the PVA. The final step involves physical debonding of the fully cured PVA film from the Si wafer at the constant peeling rate of 50 mm/min with an automated peeling apparatus (Mark-10, Willrich Precision Instrument), causing cracking to occur near the bottom undercut of the p-Si nanoneedles (Figure 1A, right).

Figure 1B provides representative photo (left) and enlarged microscope image (right) of the physically transferred p-Si nanoneedles onto a thin layer (200 μm thick) of a PVA film. The inset image highlights the sharpened angular tip of the p-Si nanoneedles, allowing for easier penetration into tissues.[28] The overall height, vertical arrangement, and tip morphology of the

transferred p-Si nanoneedles were consistent across the entire specimen area (3×3 cm^2). Figure S2 shows the fractured planes on both the donor Si wafer and the receiver PVA film, implying that the cracking occurred uniformly at the bottom undercut of the p-Si nanoneedles. Figure 1C shows the nanopores formed on the surface of the p-Si nanoneedles in which the porosity (in turn, drug loading capacity) can be adjusted during the fabrication process. The SEM images in Figure S3 provide representative examples of the p-Si nanoneedles configured with different surface porosities (0%, ~30%, ~45%, and ~60%) Figure S4 presents a series of optical images at various stages during the dissolution of the PVA film - colored with yellow food dye (McCormick & Company, USA) for visualization - when immersed in 50 ml of phosphate-buffered saline (PBS, pH 7.4, Sigma-Aldrich, USA) at 37.5°C. The complete dissolution of the PVA film occurred typically within 10-15 min in this condition, or it can be swabbed away using a saline-moistened cotton swab in less than 1 min.

The controlled cracking near the bottom undercut of the p-Si nanoneedles over centimeter-scale areas is crucial to successful implementation of this approach. Figure S5 presents an experimental setup and representative results for the peeling load–peeling distance curve for a specimen (3×3 cm^2, d = 1 μm, D = 4 μm, and L = 50 μm) under constant peeling of the PVA film at 50 mm/min. The results indicate that the peeling load was rapidly increased to a maximum and initiate cracking, and then reached a plateau for steady-state crack propagation. Figure 1D shows results of finite element analysis (FEA), revealing that the principal strain (ε) remained localized near the bottom undercut of the p-Si nanoneedles during the constant peeling. The tendency for the localization of ε was more evident as the D/d ratio was increased, wherein the peak principal strain (ε_{peak}) was larger than the fracture limit (~1%) of the Si nanoneedles when D/d>1.5 (Figure S6). The experimental and computational (FEA) results of strain energy release rate (G) for the

cracking are summarized in Figure 1E. The green-filled area defines where the cracking typically occurred with high-fidelity. Figure 1F experimentally and theoretically reveals the dependence of G on peeling rate (v) of the PVA film. The results exhibited a clear power-law relationship of them (i.e., the G was increased rapidly at low v and then gradually reached steady-state) due to the viscoelastic property of the PVA film.[29] For instance, a rapid peeling (v>20 mm/min) of the PVA film could provide sufficiently large adhesive strength to peel the p-Si nanoneedles away from the Si wafer. On the other hand, the surface of the PVA film peeled out of this condition (v<20 mm/min) showed compressed marks left behind without holding the p-Si nanoneedles (Figure S7).

Controlled dissolution of p-Si nanoneedles in biological fluids

The SEM images in Figure 2A show the gradual dissolution of a unit array (1×1 cm^2) of the p-Si nanoneedles with fixed initial base diameter (D_0) of 3 μm when immersed in 50 ml of PBS (pH 7.4) at 37.5°C for 90 days. The dissolution of the p-Si nanoneedles occurs via hydrolysis of Si to silicic acid and hydrogen (i.e., $Si + 4H_2O \leftrightarrow Si(OH)_4 + 2H_2$), which involves nucleophilic attack at the surface to weaken the interior bonds of Si atoms.[30,31] The dissolution kinetics rely on the pH, temperature, and ionic strength of the solution as well as the pre-defined surface porosity of Si.[20] Figure 2B shows measurement results for the gradual diameter reduction (D/D_0) of the p-Si nanoneedles with varied surface porosities, showing that the dissolution rate was increased from ~10 nm/day to ~20 nm/day as the surface porosity was increased from 0% to 60%. Figure 2C and D compare the dissolution of the p-Si nanoneedles in PBS (pH 10.0) at 37.5°C. The results indicate that the dissolution was substantially accelerated at higher pH while the rate was non-linearly decreased over time due to enhanced dependence on the concentration of the byproducts, such as

$Si(OH)_4$, in the solution. These experimental observations are consistent with those reported in previous articles.[20,21,31,32]

Figure 2E shows a series of snapshot images obtained from molecular dynamics (MD) simulation at different time frames, revealing the dissociation process of a Si atom (highlighted in blue) in water (H_2O) due to the effect of nucleophile attack by OH- groups (enlarged). At the beginning (t = 0.5 ns), no bonding occurred between the Si atom and OH- groups. At t = 3 ns, an OH- group started attacking the Si atom to form a bond. At t = 4 ns, another OH- group attacked the Si atom and formed another bond to break an interior Si-Si bond. At t = 6 ns, one more OH- group attacked the Si atom and finally triggered its complete dissociation. The dissociation occurred when the maximum distance of a Si atom from its nearest neighbors remained longer than 3.0Å.[31] Figure 2F shows the variation of number of dissociated Si atoms in solutions at acidic (pH 2.2) and basic (pH 10.0) conditions formed by addition of H+ and OH- groups, respectively, compared to a neutral condition (pH 7.0). The results show that the number was increased over the simulation time from 0 ns to 12 ns, while the dissolution was accelerated at higher pH due to the increased concentration of OH- groups. These findings are consistent with the above-described experimental observations.

Biocompatibility and controlled drug release

To evaluate in vivo tissue compatibility, a set of real-time bioluminescence images were captured at 5 hrs post-injection of the p-Si nanoneedles (1×1 cm^2, d = 150 nm, D = 1 μm, and L = 50 μm) to the epidermis (on top of the skin, top row) and subcutaneous muscle (under the skin, bottom row) on the backside of mice (Figure 3A). The experiments used the p-Si nanoneedles built on a medical PVA film (left column) and an industrial PVA film (Fibre Glast, USA, middle

column), as well as control treatments (right column) of phorbol 12-myristate 13-acetate (PMA; 1 mM, 20 μl, Sigma-Aldrich) that promotes intense local inflammation.[33] Both the epidermis and the subcutaneous muscle showed no evidence of inflammation following the administration of luminol (5-amino-2,3-dihydro-1,4-phthalazinedione) which detects acute inflammation at the implemented sites,[34] while acute inflammation appeared in the control mice. Here, the industrial PVA was dissolved by applying saline immediately within 1 min after the insertion of the p-Si nanoneedles into the tissues, resulting in no inflammation. Figure 3B presents in vitro cell viability of human dermal fibroblast (HDF) cells seeded in a 24-well plate (Fisher Scientific, USA) that contains the p-Si nanoneedles and the medical PVA (red bar), as measured by a colorimetric MTT assay kit (3-(4,5-Dimethylthiazol-2-yl)-2,5-diphenyltetrazolium bromide, Sigma-Aldrich, USA). The cell viability remained over 99.3% during the entire period (3 days) of the assay without substantial difference compared to that of the control bare medical PVA without p-Si nanoneedles (blue bars), while acute toxicity appeared in the industrial PVA (green bars) due to the residual ethanol and butanol. Similar results were observed in other control specimens formed by replacing the PVA film with a sheet of water-soluble poly(lactic-co-glycolic acid) (PLGA; 50/50 lactide:glycolide, molecular weight = 30,000-60,000, Sigma Aldrich, USA), exhibiting the cell viability of >97.4% (Figure S8).

Covalent conjugation of drug cargos to the surface of the p-Si nanoneedles is critical to reliable drug loading and sustained releasing behavior.[22,23] Figure 3C presents representative fluorescence microscopy images (top view) of the p-Si nanoneedles where the surface was covalently linked with chemotherapy drug doxorubicin (DOX) via 3-Triethoxysilylpropyl succinic anhydride (TESPSA, Gelest Inc., USA) as a cross-linker. The peak fluorescence intensity of the DOX was developed on the surface of the p-Si nanoneedles due to high surface area of the

nanopores. Figure 3D shows a three dimensional (3D) confocal image (tilted view) of the p-Si nanoneedles upon insertion into a soft agarose gel (2.8% w/v) with a comparable mechanical modulus (~100 kPa) to the human tissues (80-150 kPa). The experiment was performed by gently pressing the p-Si nanoneedles into the agarose gel, followed by the application of saline to completely dissolve the PVA film. The side view of the image (bottom row) highlights that the p-Si nanoneedles were embedded inside the agarose gel through the full length of 50 μm. The larger-field views of the specimen are shown in Figure S9.

Figure 3E shows the total cumulative amount of DOX released from the p-Si nanoneedles with different surface porosities of 0%-60% in PBS (pH 7.4) at 37.5°C. The corresponding release profiles as a function of time (up to 100 hrs) appear in Figure 3F, exhibiting that rapid release of DOX occurred within 24 hrs and then gradually reached a plateau at the predefined doses. The range of the released doses (18-35 μg) were comparable to those used in similar studies using conventional polymeric microneedles,[35,36] which remained higher than the half maximal inhibitory concentration (IC_{50}) value (~0.3 μg/ml) for B16F10 murine melanoma cells and substantially lower than the lethal dose (LD_{50}) value (~192 μg; green dash line) for mice. Figure 3G presents the cumulative release of covalently linked DOX with different cross-linkers of amide (red line) and urea (blue line) in PBS (pH 7.4), as compared to that of physically trapped DOX (black line), all obtained from the p-Si nanoneedles with the surface porosity of ~45%. The schematic diagrams of these bonding mechanisms are shown in Figure S10. The amide bonding showed the highest drug loading capacity (~25 μg) followed by the urea bonding (~15 μg), both of which were substantially higher than that of the physical trapping (~2 μg). These observations support that the covalently linked DOX provides strong binding affinity to the surface of the p-Si nanoneedles to form a highly stable complex at physiological pH,[37] allowing the release of the DOX to occur

exclusively when the p-Si nanoneedles are dissolved. Figure 3H presents the corresponding release profiles (%) as a function of time (up to 24 hrs), highlighting the longer-lasting release of the covalently linked DOX than counterparts. For instance, more than 80% of the covalently linked DOX was released for ~24 hrs (red and blue lines), which was substantially longer than control specimens with physically trapped DOX (~8 hrs; black line) and conventional polymeric microneedles (typically, 15 min-2 hrs [38,39]; pink-filled area), respectively.

Unobtrusive topical application of p-Si nanoneedles

To illuminate its utility in the envisioned scenarios of transepidermal, transmuscular, and transocular injections, a unit array (1×1 cm^2) of p-Si nanoneedles (d = 150 nm, D = 1 μm, and L = 50 μm) with covalently (amide) linked fluorescent dyes (DyLight 800, Pierce Thermo Scientific) was introduced onto the epidermis, subcutaneous muscle, and cornea of athymic nude mice in vivo. Details of the experimental procedures are shown in the Methods section. Figure 4A shows optical images pointing out the injection sites where the p-Si nanoneedles were embedded inside the tissues after the PVA film was completely dissolved by the application of saline. The size of the p-Si nanoneedles was substantially small compared with that of conventional polymeric microneedles (typically, d>5 μm, D>300 μm, and L>600 μm),[9,40] and remained nearly unnoticeable on the tissue surface by visual observations (Figure S11). This aspect can potentially reduce the risk of pain and irritation during/after the injection of the p-Si nanoneedles. The mice exhibited normal behavior without showing any evidence of discomfort against natural movements for the entire period of observation (>3 months). Figure 4B shows the corresponding IVIS images indicating that the fluorescent dyes were uniformly localized over the curvilinear surface of the epidermis, subcutaneous muscle, and cornea of the mice, and maintained until the absorption of

the florescent dyes throughout the body was completed. Figure S12 shows optical images of a control unit array (1×1 cm^2) of the p-Si nanoneedles built on a flexible, transparent, and non-water-soluble backing film such as PDMS (200 μm thick), which was attached on the back of a nude mouse. Of note, no skin wrinkles were observed over the PDMS while other areas of the skin were easily wrinkled according to body movements. These observations imply that the skin underneath the PDMS experienced occasional irritations and interruptions due to the physical constraints.

Demonstration on post-surgical melanoma treatments in mice in vivo

Tumor relapse after surgical resection, frequently resulting from the outgrowth of residual microtumors, remains a significant challenge in the treatment.[41,42] Systematic chemotherapy and radiotherapy are often employed to prevent the recurrence of residual tumors, but these methods may lead to toxic side effects.[43] Sustained local delivery of therapeutic drug cargos with precisely controlled doses for a prolonged time, after surgical resection, may reduce the risk of tumor relapse with minimal side effects.

To demonstrate the utility of the p-Si nanoneedles in the inhibition of post-surgical residual melanoma, C57BL/6 mice were administered with an array (1×1 cm^2) of the p-Si nanoneedles (d = 150 nm, D = 1 μm, and L = 50 μm) covalently (amide) linked with 50 μl of DOX (~20 μg) or without DOX (control) after 2 hrs of subcutaneous inoculation with 1×10^6 B16F10 melanoma cells (Figure 5A). A representative photo in Figure 5B highlights the injection site on the shaved skin of a mouse. The mouse receiving the p-Si nanoneedles moved freely without any sign of discomfort. Two other control groups of mice were intratumorally administered using a medical 28G insulin syringe (Fisher Scientific, USA) with a single dose of PBS (50 μl) and DOX (50 μl), respectively. Figure 5C shows that, in the mice treated with the nanoinjection of DOX, tumor

growth was suppressed over 10 days post-inoculation. In contrast, significant growth of the tumors occurred in 4 out of 5 mice treated with the control nanoinjection (without DOX), all 5 mice with the syringe injection of PBS, and 4 out of 5 mice with the syringe injection of DOX during the same period, followed by rapid increase to reach the endpoint tumor size of 2,000 mm3 (Figure S13).[44,45] Figure 5D presents a scatter plot comparing the size of the tumors at 10 days post-inoculation. All the treatments were well tolerated with negligible weight loss during the surviving period (Figure 5E). Of note, severe local skin lesions were observed on the mice treated with the syringe injection of DOX, a typical side effect of the drug (Figure 5F & Figure S14).[46] These findings support that the nanoinjection of the DOX enabled the unobtrusive, effective local delivery of chemotherapeutics to melanoma without adverse effects.

CONCLUSION

Exploiting concentrated cracking phenomenon near the bottom undercut of vertically ordered p-Si nanoneedles enables their controlled separation from the fabrication Si wafer and subsequent integration with a water-soluble medical film over centimeter-scale areas. The water-soluble film serves as a temporary holder that can be flexibly interfaced with the soft, curvilinear surface of living tissues during the insertion of the p-Si nanoneedles, followed by rapid, complete dissolution within one minute. The nanoscale size and sharpened angular tip of the p-Si nanoneedles facilitate to penetrate the epidermis, subcutaneous muscle, and cornea of mice in vivo in a minimally invasive manner, and then can be gradually degraded in tissue fluids, resulting in sustained, long-lasting release of preloaded drug cargos. In vivo studies with a murine melanoma model support potential utility of this concept in the local prevention of melanoma growth. Further investigations to evaluate the pre-clinical efficacy in preventing the recurrence of residual

melanoma post-surgery are warranted in the future. The established set of materials, structural designs, and assembly method provides a foundation, which can be adjusted and tailored for the painless nanoinjection of various drug cargos through small, curvilinear, or/and sensitive areas of tissues, such as cornea (for the treatment of chronic ocular diseases).[47,48]

MATERIALS AND METHODS

Fabrication of p-Si nanoneedles on a Si wafer. The fabrication began with a bulk Si wafer (p-type, 525 μm thick, 0-100 Ω·cm) by immersing it in a solution of buffered oxide etch (J. T. Baker Inc., USA) for 1 min to eliminate the native oxide layer. A deep reactive-ion etching (DRIE) following a standard photolithographic patterning was carried out under a radiofrequency (RF) plasma power of 450W and a platen power of 11W using sulfur hexafluoride (SF_6) gas with a flow rate of 85 sccm to create vertically ordered Si micropillars with prescribed aspect ratios, followed by a deposition of $(C_xF_y)n$ polymer to form a partial passivation layer using octafluorocyclobutane (C_4F_8) gas with a flow rate of 130 sccm under a RF plasma power of 800W. Additional isotropic dry etching under the plasma power of 450W and a platen power of 30W by SF_6 gas with a flow rate 85 sccm was conducted to create undercuts at the bottom of the Si micropillars. The entire specimen underwent an oxygen (O_2) plasma treatment (20 sccm, 150W, 50 mtorr, 15 min), followed by a standard piranha cleaning (75% of sulfuric acid (H_2SO_4) and 25% of hydrogen peroxides (H_2O_2)) to eliminate the remaining passivation layer on the surface of the Si micropillars. Finally, the entire specimen was immersed in a solution of potassium hydroxide (KOH; 15 weight %, Fisher Scientific, USA) at 25°C to reduce the overall size of the Si micropillars down to the nanoscale (Si nanoneedles). The overall size of the resulting Si nanoneedles was determined by controlling the molarity of etching solution, temperature, and etching time (**27**). The specimen was

then immersed in a mixed solution of 20 mM silver nitrate ($AgNO_3$; Sigma-Aldrich, USA) and 49% hydrofluoric acid (HF; J. T. Baker Inc., USA) to form nanopores on the surface. The overall porosity was determined by controlling the molarity of etching solution, temperature, and etching time.49 The specimen was then immersed in a solution of Ag etchant (TFS, KI-I2 complex liquid, Transene Inc., USA) for 1 min to remove the remaining Ag residues on the surface. The surface property of the resulting p-Si nanoneedles was characterized using a high-resolution SEM (S-4800, Hitachi, Japan) and post-image processing (Stream Desktop 2.1, Olympus, Japan).

Integration of p-Si nanoneedles with water-soluble medical film. The process began by defining a spin-cast, pre-cured solution of 10 weight % PVA (Mowiol 4-88; Sigma Aldrich, USA) or 5.5 weight % PLGA (lactide:glycolide (50:50); Sigma Aldrich, USA) on the as-fabricated p-Si nanoneedles, followed by complete curing at 70°C for 30 min. At this stage, the thickness of the water-soluble (PVA or PLGA) film was determined by adjusting the spin-casting speed (in rpm) and repeating the casting cycles. Finally, the film was mechanically peeled using an automated peeling apparatus (Mark-10, Willrich Precision Instrument) at constant rate of 50 mm/min, causing cracking at the bottom undercut of the p-Si nanoneedles.

Calculation of theoretical strain energy release rate (G). By measuring the peeling force at low velocity near zero, the theoretical energy release rate was calculated according to the peeling rate. In the steady-state crack propagation, the strain energy release rate (G) has the following relation by [54]

$$G = \frac{F}{w} \quad (1)$$

where F is measured peel force and w is width of the PVA film. By calculating the critical energy release rate (G_0) at the reference velocity (v_0) near zero, theoretical energy release rate can be determined as power law equation,[55]

$$G = G_0 \left[1 + \left(\frac{v}{v_0}\right)^n\right] \quad (2)$$

where n is experimentally measured constant. In the peeling tests, the range of the peeling rate of 2.4-200 mm/min, critical energy release rate (G_0) of 26.15 J/m^2, reference velocity (v_0) of 2.4 mm/min, and experimental constant (n) of 0.14 were determined.

Finite element analysis (FEA). The FEA was conducted using the ABAQUS/standard package to reveal the underlying mechanics of p-Si nanoneedles under mechanical peeling process. The deformation of p-Si nanoneedles and PVA film was modeled by linear elastic behavior with the mechanical modulus (E) of 112.4 GPa and 3.4 GPa, respectively.[50,51] The materials were modeled by 8 nodes solid elements (C_3D_8R). The displacement at constant peeling rate was applied on the top of the PVA film while a tie constraint was defined at the interface between the p-Si nanoneedles and the PVA film.

Loading of DOX on the surface of p-Si nanoneedles. The process began by washing the as-fabricated p-Si nanoneedles on a Si wafer with distilled (DI) water, followed by thorough drying

with nitrogen gas. The cleaned p-Si nanoneedles were immersed in a solution of 3-Triethoxysilylpropyl succinic anhydride (TESPSA, Gelest Inc., USA) for 2 hrs to functionalize the surface with amide bond.[52] Alternatively, the p-Si nanoneedles were immersed in a solution of 3-Triethoxysilylpropyl isocyanate (ICPTS, Sigma-Aldrich, USA) for 2 hrs to functionalize the surface with urea bond.[53] The p-Si nanoneedles were then rinsed with ethanol and then baked at 120°C for 1 hr, followed by immersion in a solution of DOX (0.5 mg/ml; Sigma-Aldrich, USA) for 24 hrs at room temperature. To prepare the control specimens with physically trapped DOX, the as-fabricated p-Si nanoneedles were immersed in a solution of DOX without undergoing any treatment on the surface. The prepared specimens were dried by nitrogen gas and stored under an inert atmosphere.

Measurement of cumulative DOX release. The p-Si nanoneedles loaded with DOX were immersed in PBS (pH 7.4 or pH 10.0; Sigma-Aldrich, USA) at 37.5°C. At predetermined time intervals, the specimens were sampled, and the solution was replaced with fresh PBS solution. A 100 µl of the sampled solution was transferred to a 96-well plate, and the fluorescent intensity was measured with a plate reader (Synergy Neo Plate Reader, BioTek Instruments). The concentration of the DOX released from the p-Si nanoneedles was determined according to the fluorescent intensity measured with excitation at 480 nm and emission at 600 nm.[56]

Molecular dynamics (MD) simulation. The MD simulations were conducted to model atomic scale chemical interactions of Si with H2O and associated dissolution dynamics with the Reaxff potential,[57] integrated in the large-scale atomic/molecular massively parallel simulator (LAMMPS) package. In the simulations, Si, O, and H were used for the atomic elements.[58] The initial systems included a Si layer with a thickness of 1.2 nm, which was solvated by a box of H_2O

with 3090 water molecules. Periodic boundary conditions were used in all directions. The temperature of the system was maintained at T = 300K using Nose-Hoover thermostat, and the time step was selected to be 0.1 fs, to order to ensure the capture of chemical reaction events between the Si and H_2O species.

Cell viability test. For the MTT assay, approximately 5×10^4 human dermal fibroblast (HDF) cells were seeded on specimens in a 24-well plate and then incubated for 24 hrs, 48 hrs, and 72 hrs. At each measurement point, 200 μl of MTT solution ((3-(4,5-dimethylthiazol-2-yl)-2,5-diphenyltetrazolium bromide); Sigma-Aldrich, USA) was added to the wells and incubated for 4 hrs. The cell medium was removed, and 400 μl of dimethyl sulfoxide (C_2H_6OH; Sigma-Aldrich, USA) was added to dissolve precipitated formazan. A 100 μl of the solution was transferred to a 96-well plate and measured with a microplate reader (SpectraMax Plus 384 reader, Molecular Devices, USA) at 570 nm.

Acute inflammation test in vivo. All the animal procedures were approved by the Purdue Animal Care and Use Committee (PACUC; #1612001512) for the care and use of laboratory animals. Female athymic nude mice (5-6 weeks old; NCr-Fox1nu, Charles River Laboratories, USA) were used in the acute inflammation tests in vivo. As a positive control, 40 μl of PMA (100 μM; Sigma-Aldrich, USA) was rubbed on the epidermis and subcutaneous muscle to induce acute inflammation.[34] The p-Si nanoneedles on water-soluble backing were gently applied to the target sites with firm compression. The backing film was then completely dissolved by applying a saline-moistened cotton swab. Following 5 hrs of the implementation, 100 μl of luminol sodium salt (200 mg/kg; Sigma-Aldrich, USA) was administered by the intraperitoneal nanoinjection. Then, the

mice were anesthetized with compressed air containing 2.5% isoflurane with a Classic T3 isoflurane vaporizer (Smith Medical, Dublin, OH). Bioluminescence images were acquired with an IVIS Lumina II imaging system (Caliper Life Sciences, USA) for 3 min of the exposure time, with F/stop = 1 and binning = 4.

IVIS imaging in vivo. All the animal procedures were approved by the Purdue Animal Care and Use Committee (PACUC; #1612001512). The p-Si nanoneedles with covalently (amide) linked DyLight 800 dyes were placed either on the epidermis, subcutaneous muscle, and cornea of mice (5-6 weeks old; NCr-Fox1nu, Charles River Laboratories, USA) with firm compression. For the transmuscular nanoinjection, 250 mg/kg of avertin (Sigma-Aldrich, USA) was administrated by intraperitoneal injection to anesthetize mice, followed by careful incision of the skin with surgical scissors. The incisional site was then sutured using surgical needle and thread. The mice were anesthetized with inhaled isoflurane anesthesia with a Classic T3 isoflurane vaporizer (Smith Medical, Dublin, OH) and exposed to 2.5% isoflurane delivered in O_2 (2 litters/min) within a 1-litter induction chamber. The fluorescence of the injection site was measured with an IVIS Lumina II imaging system (Caliper Life Sciences, USA) at the day 0, 1, and 2 with the exposure time of 1 sec each with a 150W quartz halogen lamp, and then filtered using an indocyanine green (ICG) excitation filter with the wavelength of 710-760 nm and an ICG emission filter with the wavelength of 810-875 nm. Data analysis was performed with the Living Image software (version 4.4, PerkinElmer Inc).

Demonstration in a murine melanoma model. All the animal procedures were approved by the Purdue Animal Care and Use Committee (PACUC; #1503001212). Male C57BL/6 mice (8-10

weeks old; Envigo, USA) were acclimatized for at least 1 week prior to the procedures. The specimens were sterilized by an ultraviolet (UV) illumination (254 nm) for 30 min. 10^6 B16F10 melanoma cells (ATCC; Manassas, VA, USA) were subcutaneously inoculated in the bottom flank of the right hind leg of each mouse. After approximately 2 hrs, the inoculation site was treated with the nanoinjection of the covalently (amide) linked DOX (~20 μg) and the control nanoinjection (without DOX). For comparison, two other control groups of mice were intratumorally administered using a medical 28G insulin syringe (Fisher, USA) with a single dose of PBS (50 μl) and DOX (20 μg in 50 μl), respectively. The length (L) and width (W) of each tumor were monitored every day using a digital caliper (Thorlabs Digital Calipers, Thorlabs Inc, USA), and the volume (V) was calculated according to an ellipsoid formula: $V = (L \times W^2)/2$. The body weight of the mice was monitored every other day.

ASSOCIATED CONTENT

Supporting Information.

SEM images of p-Si nanoneedles fabricated on a Si wafer with varied sizes (Figure S1); SEM images of representative donor Si wafer and receiver PVA film (Figure S2); SEM images of p-Si nanoneedles with different surface porosities (Figure S3); time-dependent optical images of a yellow-colored PVA film (Figure S4); optical image and measurement of peeling of p-Si nanoneedles (Figure S5); computational (FEA) results displaying the distribution of principal strains (Figure S6); representative SEM image displaying the compressed marks leftover on the surface of a PVA film (Figure S7); photo and SEM images of p-Si nanoneedles built on a water-soluble PLGA film and results of MTT assay in the cytotoxicity tests of HDF cells (Figure S8); microscope images of p-Si nanoneedles embedded inside a 2.8% (w/v) agarose gel (Figure S9); schematic illustration of amide bonding, urea bonding, and physical trapping of DOX on the surface of a single p-Si nanoneedle (Figure S10); enlarged optical images of the epidermis, subcutaneous muscle, and cornea of mice receiving an array of p-Si nanoneedles (Figure S11); optical images of p-Si nanoneedles built on a PDMS film and attached on the backside of a nude mouse (Figure S12); measurement results for the growth of tumor size (Figure S13); enlarged optical images of the treated location of the mice at 10 days post-injection (Figure S14).

REFERENCES

1. Simoes, M. C. F.; Sousa, J. J. S.; Pais, A. A. C. C., Skin cancer and new treatment perspectives: A review. *Cancer Letters* **2015,** *357* (1), 8-42.
2. Kottmann, J.; Rey, J. M.; Sigrist, M. W., Mid-Infrared Photoacoustic Detection of Glucose in Human Skin: Towards Non-Invasive Diagnostics. *Sensors* **2016,** *16* (10).
3. Perera, E.; Gnaneswaran, N.; Jennens, R.; Sinclair, R., Malignant Melanoma. *Healthcare* **2014,** *2* (1), 1-19.
4. Prausnitz, M. R.; Langer, R., Transdermal drug delivery. *Nature Biotechnology* **2008,** *26* (11), 1261-1268.
5. Anselmo, A. C.; Gokarn, Y.; Mitragotri, S., Non-invasive delivery strategies for biologics. *Nature Reviews Drug Discovery* **2019,** *18* (1), 19-40.
6. Lee, H.; Song, C.; Baik, S.; Kim, D.; Hyeon, T.; Kim, D. H., Device-assisted transdermal drug delivery. *Advanced Drug Delivery Reviews* **2018,** *127*, 35-45.
7. Dagdeviren, C.; Ramadi, K. B.; Joe, P.; Spencer, K.; Schwerdt, H. N.; Shimazu, H.; Delcasso, S.; Amemori, K. I.; Nunez-Lopez, C.; Graybiel, A. M.; Cima, M. J.; Langer, R., Miniaturized neural system for chronic, local intracerebral drug delivery. *Science Translational Medicine* **2018,** *10* (425).
8. Li, W.; Terry, R. N.; Tang, J.; Feng, M. H. R.; Schwendeman, S. P.; Prausnitz, M. R., Rapidly separable microneedle patch for the sustained release of a contraceptive. *Nature Biomedical Engineering* **2019,** *3* (3), 220-+.
9. Chen, M. C.; Lin, Z. W.; Ling, M. H., Near-Infrared Light-Activatable Microneedle System for Treating Superficial Tumors by Combination of Chemotherapy and Photothermal Therapy. *Acs Nano* **2016,** *10* (1), 93-101.

10. Wang, C.; Ye, Y. Q.; Hochu, G. M.; Sadeghifar, H.; Gu, Z., Enhanced Cancer Immunotherapy by Microneedle Patch-Assisted Delivery of Anti-PD1 Antibody. *Nano Letters* **2016,** *16* (4), 2334-2340.
11. Ye, Y. Q.; Wang, C.; Zhang, X. D.; Hu, Q. Y.; Zhang, Y. Q.; Liu, Q.; Wen, D.; Milligan, J.; Bellotti, A.; Huang, L.; Dotti, G.; Gu, Z., A melanin-mediated cancer immunotherapy patch. *Science Immunology* **2017,** *2* (17).
12. Sullivan, S. P.; Koutsonanos, D. G.; Martin, M. D.; Lee, J. W.; Zarnitsyn, V.; Choi, S. O.; Murthy, N.; Compans, R. W.; Skountzou, I.; Prausnitz, M. R., Dissolving polymer microneedle patches for influenza vaccination. *Nature Medicine* **2010,** *16* (8), 915-U116.
13. Gopal, S.; Chiappini, C.; Penders, J.; Leonardo, V.; Seong, H.; Rothery, S.; Korchev, Y.; Shevchuk, A.; Stevens, M. M., Porous Silicon Nanoneedles Modulate Endocytosis to Deliver Biological Payloads. *Advanced Materials* **2019,** *31* (12).
14. Chiappini, C.; De Rosa, E.; Martinez, J. O.; Liu, X.; Steele, J.; Stevens, M. M.; Tasciotti, E., Biodegradable silicon nanoneedles delivering nucleic acids intracellularly induce localized in vivo neovascularization. *Nature Materials* **2015,** *14* (5), 532-539.
15. Chiappini, C.; Martinez, J. O.; De Rosa, E.; Almeida, C. S.; Tasciotti, E.; Stevens, M. M., Biodegradable Nanoneedles for Localized Delivery of Nanoparticles in Vivo: Exploring the Biointerface. *Acs Nano* **2015,** *9* (5), 5500-5509.
16. Shalek, A. K.; Robinson, J. T.; Karp, E. S.; Lee, J. S.; Ahn, D. R.; Yoon, M. H.; Sutton, A.; Jorgolli, M.; Gertner, R. S.; Gujral, T. S.; MacBeath, G.; Yang, E. G.; Park, H., Vertical silicon nanowires as a universal platform for delivering biomolecules into living cells. *Proceedings of the National Academy of Sciences of the United States of America* **2010,** *107* (5), 1870-1875.

17. Fang, Y.; Jiang, Y. W.; Ledesrna, H. A.; Yi, J. S.; Gao, X.; Weiss, D. E.; Shi, F. Y.; Tian, B. Z., Texturing Silicon Nanowires for Highly Localized Optical Modulation of Cellular Dynamics. *Nano Letters* **2018,** *18* (7), 4487-4492.
18. Luo, Z. Q.; Jiang, Y. W.; Myers, B. D.; Isheim, D.; Wu, J. S.; Zimmerman, J. F.; Wang, Z. G.; Li, Q. Q.; Wang, Y. C.; Chen, X. Q.; Dravid, V. P.; Seidman, D. N.; Tian, B. Z., Atomic gold-enabled three-dimensional lithography for silicon mesostructures. *Science* **2015,** *348* (6242), 1451-1455.
19. Chiappini, C.; Campagnolo, P.; Almeida, C. S.; Abbassi-Ghadi, N.; Chow, L. W.; Hanna, G. B.; Stevens, M. M., Mapping Local Cytosolic Enzymatic Activity in Human Esophageal Mucosa with Porous Silicon Nanoneedles. *Advanced Materials* **2015,** *27* (35), 5147-5152.
20. Lee, Y. K.; Yu, K. J.; Song, E. M.; Farimani, A. B.; Vitale, F.; Xie, Z. Q.; Yoon, Y.; Kim, Y.; Richardson, A.; Luan, H. W.; Wu, Y. X.; Xie, X.; Lucas, T. H.; Crawford, K.; Mei, Y. F.; Feng, X.; Huang, Y. G.; Litt, B.; Aluru, N. R.; Yin, L.; Rogers, J. A., Dissolution of Monocrystalline Silicon Nanomembranes and Their Use as Encapsulation Layers and Electrical Interfaces in Water-Soluble Electronics. *Acs Nano* **2017,** *11* (12), 12562-12572.
21. Hwang, S. W.; Park, G.; Edwards, C.; Corbin, E. A.; Kang, S. K.; Cheng, H. Y.; Song, J. K.; Kim, J. H.; Yu, S.; Ng, J.; Lee, J. E.; Kim, J.; Yee, C.; Bhaduri, B.; Su, Y.; Omennetto, F. G.; Huang, Y. G.; Bashir, R.; Goddard, L.; Popescu, G.; Lee, K. M.; Rogers, J. A., Dissolution Chemistry and Biocompatibility of Single-Crystalline Silicon Nanomembranes and Associated Materials for Transient Electronics. *Acs Nano* **2014,** *8* (6), 5843-5851.
22. Anglin, E. J.; Cheng, L. Y.; Freeman, W. R.; Sailor, M. J., Porous silicon in drug delivery devices and materials. *Advanced Drug Delivery Reviews* **2008,** *60* (11), 1266-1277.

23. Santos, H. A.; Makila, E.; Airaksinen, A. J.; Bimbo, L. M.; Hirvonen, J., Porous silicon nanoparticles for nanomedicine: preparation and biomedical applications. *Nanomedicine* **2014,** *9* (4), 535-554.

24. Abbott, J.; Ye, T. Y.; Ham, D.; Park, H., Optimizing Nanoelectrode Arrays for Scalable Intracellular Electrophysiology. *Accounts of Chemical Research* **2018,** *51* (3), 600-608.

25. Abbott, J.; Ye, T. Y.; Qin, L.; Jorgolli, M.; Gertner, R. S.; Ham, D.; Park, H., CMOS nanoelectrode array for all-electrical intracellular electrophysiological imaging. *Nature Nanotechnology* **2017,** *12* (5), 460-466.

26. Jovanovic, P.; Mihajlovic, M.; Djordjevic-Jocic, J.; Vlajkovic, S.; Cekic, S.; Stefanovic, V., Ocular melanoma: an overview of the current status. *International Journal of Clinical and Experimental Pathology* **2013,** *6* (7), 1230-1244.

27. Kim, H.; Jang, H.; Kim, B.; Kim, M. K.; Wie, D. S.; Lee, H. S.; Kim, D. R.; Lee, C. H., Flexible elastomer patch with vertical silicon nanoneedles for intracellular and intratissue nanoinjection of biomolecules. *Science Advances* **2018,** *4* (11).

28. Lim, J.; Tahk, D.; Yu, J.; Min, D. H.; Jeon, N. L., Design rules for a tunable merged-tip microneedle. *Microsystems & Nanoengineering* **2018,** *4*.

29. Meitl, M. A.; Zhu, Z. T.; Kumar, V.; Lee, K. J.; Feng, X.; Huang, Y. Y.; Adesida, I.; Nuzzo, R. G.; Rogers, J. A., Transfer printing by kinetic control of adhesion to an elastomeric stamp. *Nature Materials* **2006,** *5* (1), 33-38.

30. Wang, L.; Gao, Y.; Dai, F. Q.; Kong, D. Y.; Wang, H. C.; Sun, P. C.; Shi, Z.; Sheng, X.; Xu, B. X.; Yin, L., Geometrical and Chemical-Dependent Hydrolysis Mechanisms of Silicon Nanomembranes for Biodegradable Electronics. *Acs Applied Materials & Interfaces* **2019,** *11* (19), 18013-18023.

31. Yin, L.; Farimani, A. B.; Min, K.; Vishal, N.; Lam, J.; Lee, Y. K.; Aluru, N. R.; Rogers, J. A., Mechanisms for Hydrolysis of Silicon Nanomembranes as Used in Bioresorbable Electronics. *Advanced Materials* **2015,** *27* (11), 1857-+.

32. Hwang, S. W.; Park, G.; Cheng, H.; Song, J. K.; Kang, S. K.; Yin, L.; Kim, J. H.; Omenetto, F. G.; Huang, Y. G.; Lee, K. M.; Rogers, J. A., 25th Anniversary Article: Materials for High-Performance Biodegradable Semiconductor Devices. *Advanced Materials* **2014,** *26* (13), 1992-2000.

33. Muller, A. J.; Sharma, M. D.; Chandler, P. R.; DuHadaway, J. B.; Everhart, M. E.; Johnson, B. A.; Kahler, D. J.; Pihkala, J.; Soler, A. P.; Munn, D. H.; Prendergast, G. C.; Mellor, A. L., Chronic inflammation that facilitates tumor progression creates local immune suppression by inducing indoleamine 2,3 dioxygenase. *Proceedings of the National Academy of Sciences of the United States of America* **2008,** *105* (44), 17073-17078.

34. Gross, S.; Gammon, S. T.; Moss, B. L.; Rauch, D.; Harding, J.; Heinecke, J. W.; Ratner, L.; Piwnica-Worms, D., Bioluminescence imaging of myeloperoxidase activity in vivo. *Nature Medicine* **2009,** *15* (4), 455-461.

35. Pei, P.; Yang, F.; Liu, J. X.; Hu, H. R.; Du, X. Y.; Hanagata, N.; Zhao, S. C.; Zhu, Y. F., Composite-dissolving microneedle patches for chemotherapy and photothermal therapy in superficial tumor treatment. *Biomaterials Science* **2018,** *6* (6), 1414-1423.

36. Ahmed, K. S.; Shan, X. T.; Mao, J.; Qiu, L. P.; Chen, J. H., Derma roller (R) microneedles-mediated transdermal delivery of doxorubicin and celecoxib co-loaded liposomes for enhancing the anticancer effect. *Materials Science & Engineering C-Materials for Biological Applications* **2019,** *99*, 1448-1458.

37. Wu, E. C.; Park, J. H.; Park, J.; Segal, E.; Cunin, F.; Sailor, M. J., Oxidation-Triggered Release of Fluorescent Molecules or Drugs from Mesoporous Si Microplarticles. *Acs Nano* **2008,** *2* (11), 2401-2409.

38. Yang, H. J.; Wu, X. J.; Zhou, Z. Z.; Chen, X. G.; Kong, M., Enhanced transdermal lymphatic delivery of doxorubicin via hyaluronic acid based transfersomes/microneedle complex for tumor metastasis therapy. *International Journal of Biological Macromolecules* **2019,** *125*, 9-16.

39. Bhatnagar, S.; Bankar, N. G.; Kulkarni, M. V.; Venuganti, V. V. K., Dissolvable microneedle patch containing doxorubicin and docetaxel is effective in 4T1 xenografted breast cancer mouse model. *International Journal of Pharmaceutics* **2019,** *556*, 263-275.

40. Chen, M. C.; Huang, S. F.; Lai, K. Y.; Ling, M. H., Fully embeddable chitosan microneedles as a sustained release depot for intradermal vaccination. *Biomaterials* **2013,** *34* (12), 3077-3086.

41. Chen, Q.; Wang, C.; Zhang, X. D.; Chen, G. J.; Hu, Q. Y.; Li, H. J.; Wang, J. Q.; Wen, D.; Zhang, Y. Q.; Lu, Y. F.; Yang, G.; Jiang, C.; Wang, J.; Dotti, G.; Gu, Z., In situ sprayed bioresponsive immunotherapeutic gel for post-surgical cancer treatment. *Nature Nanotechnology* **2019,** *14* (1), 89-+.

42. Wang, C.; Sun, W. J.; Ye, Y. Q.; Hu, Q. Y.; Bomba, H. N.; Gu, Z., In situ activation of platelets with checkpoint inhibitors for post-surgical cancer immunotherapy. *Nature Biomedical Engineering* **2017,** *1* (2).

43. Albain, K. S.; Swann, R. S.; Rusch, V. W.; Turrisi, A. T.; Shepherd, F. A.; Smith, C.; Chen, Y.; Livingston, R. B.; Feins, R. H.; Gandara, D. R.; Fry, W. A.; Darling, G.; Johnson, D. H.; Green, M. R.; Miller, R. C.; Ley, J.; Sause, W. T.; Cox, J. D., Radiotherapy plus chemotherapy

with or without surgical resection for stage III non-small-cell lung cancer: a phase III randomised controlled trial. *Lancet* **2009,** *374* (9687), 379-386.

44. Wong, H.; Choo, E. F.; Alicke, B.; Ding, X.; La, H.; McNamara, E.; Theil, F. P.; Tibbitts, J.; Friedman, L. S.; Hop, C. E. C. A.; Gould, S. E., Antitumor Activity of Targeted and Cytotoxic Agents in Murine Subcutaneous Tumor Models Correlates with Clinical Response. *Clinical Cancer Research* **2012,** *18* (14), 3846-3855.
45. Xu, J.; Lee, S. S. Y.; Seo, H.; Pang, L.; Jun, Y.; Zhang, R. Y.; Zhang, Z. Y.; Kim, P.; Lee, W.; Kron, S. J.; Yeo, Y., Quinic Acid-Conjugated Nanoparticles Enhance Drug Delivery to Solid Tumors via Interactions with Endothelial Selectins. *Small* **2018,** *14* (50).
46. Kubicka-Wolkowska, J.; Kedzierska, M.; Lisik-Habib, M.; Potemski, P., Skin toxicity in a patient with ovarian cancer treated with pegylated liposomal doxorubicin: A case report and review of the literature. *Oncology Letters* **2016,** *12* (6), 5332-5334.
47. Than, A.; Liu, C. H.; Chang, H.; Duong, P. K.; Cheung, C. M. G.; Xu, C. J.; Wang, X. M.; Chen, P., Self-implantable double-layered micro-drug-reservoirs for efficient and controlled ocular drug delivery. *Nature Communications* **2018,** *9*.
48. Sassalos, T. M.; Paulus, Y. M., Prefilled syringes for intravitreal drug delivery. *Clinical Ophthalmology* **2019,** *13*, 701-706.
49. Han, H.; Huang, Z. P.; Lee, W., Metal-assisted chemical etching of silicon and nanotechnology applications. *Nano Today* **2014,** *9* (3), 271-304.
50. Ryu, S. Y.; Xiao, J. L.; Il Park, W.; Son, K. S.; Huang, Y. Y.; Paik, U.; Rogers, J. A., Lateral Buckling Mechanics in Silicon Nanowires on Elastomeric Substrates. *Nano Letters* **2009,** *9* (9), 3214-3219.

51. Bermejo, J. S.; Ugarte, C. M., Influence of Cross-Linking Density on the Glass Transition and Structure of Chemically Cross-Linked PVA: A Molecular Dynamics Study. *Macromolecular Theory and Simulations* **2009,** *18* (6), 317-327.

52. Gang, A.; Gabernet, G.; Renner, L. D.; Baraban, L.; Cuniberti, G., A simple two-step silane-based (bio-) receptor molecule immobilization without additional binding site passivation. *Rsc Advances* **2015,** *5* (45), 35631-35634.

53. Escorihuela, J.; Banuls, M. J.; Castello, J. G.; Toccafondo, V.; Garcia-Ruperez, J.; Puchades, R.; Maquieira, A., Chemical silicon surface modification and bioreceptor attachment to develop competitive integrated photonic biosensors. *Analytical and Bioanalytical Chemistry* **2012,** *404* (10), 2831-2840.

54. Feng, X.; Meitl, M. A.; Bowen, A. M.; Huang, Y.; Nuzzo, R. G.; Rogers, J. A., Competing fracture in kinetically controlled transfer printing. *Langmuir* **2007,** *23* (25), 12555-12560.

55. Chen, H.; Feng, X.; Huang, Y.; Huang, Y. G.; Rogers, J. A., Experiments and viscoelastic analysis of peel test with patterned strips for applications to transfer printing. *Journal of the Mechanics and Physics of Solids* **2013,** *61* (8), 1737-1752.

56. Shah, S.; Chandra, A.; Kaur, A.; Sabnis, N.; Lacko, A.; Gryczynski, Z.; Fudala, R.; Gryczynski, I., Fluorescence properties of doxorubicin in PBS buffer and PVA films. *Journal of Photochemistry and Photobiology B-Biology* **2017,** *170*, 65-69.

57. Zhang, Y.; Kim, B. O. O.; Gao, Y.; Wie, D. S.; Lee, C. H.; Xu, B. X., Chemomechanics of transfer printing of thin films in a liquid environment. *International Journal of Solids and Structures* **2019,** *180*, 30-44.

58. Fogarty, J. C.; Aktulga, H. M.; Grama, A. Y.; van Duin, A. C. T.; Pandit, S. A., A reactive molecular dynamics simulation of the silica-water interface. *Journal of Chemical Physics* **2010,** *132* (17).

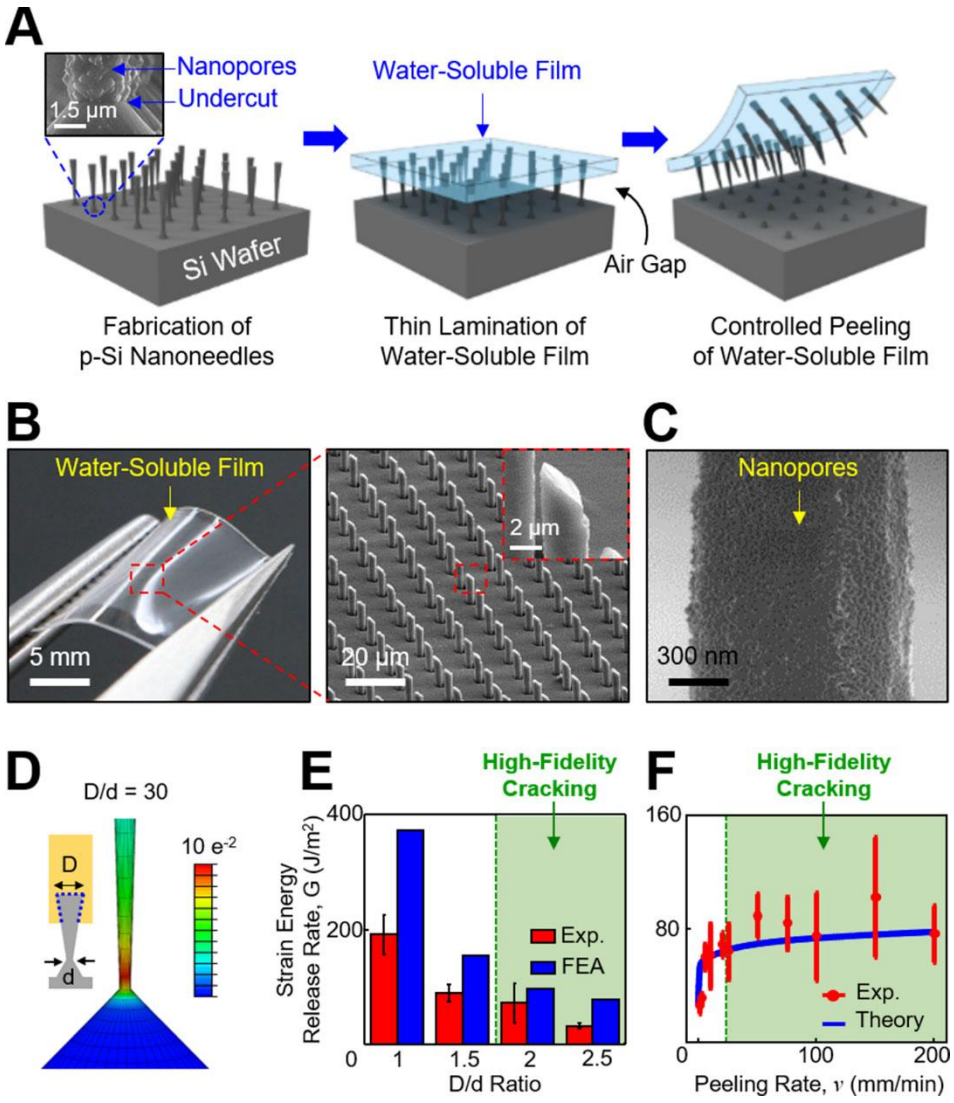

Figure 1. Design principle and fabrication process. (A) Schematic illustration for the construction of p-Si nanoneedles on water-soluble backing. The inset image highlights the bottom undercuts and nanopores at the bottom and on the surface of the p-Si nanoneedles, respectively. (B) Optical images of the p-Si nanoneedles integrated with a water-soluble PVA film. The inset image highlights the sharpened angular tip of the p-Si nanoneedles. (C) SEM image of the nanopores formed on the surface of the p-Si nanoneedles. (D) Representative FEA results showing the distribution of principal strains along a single p-Si nanoneedle during constant peeling. (E) Experimental and computational (FEA) results for the effect of D/d ratio on strain energy release rate (G). (F) Experimental and theoretical results for the effect of peeling rate (v) on G.

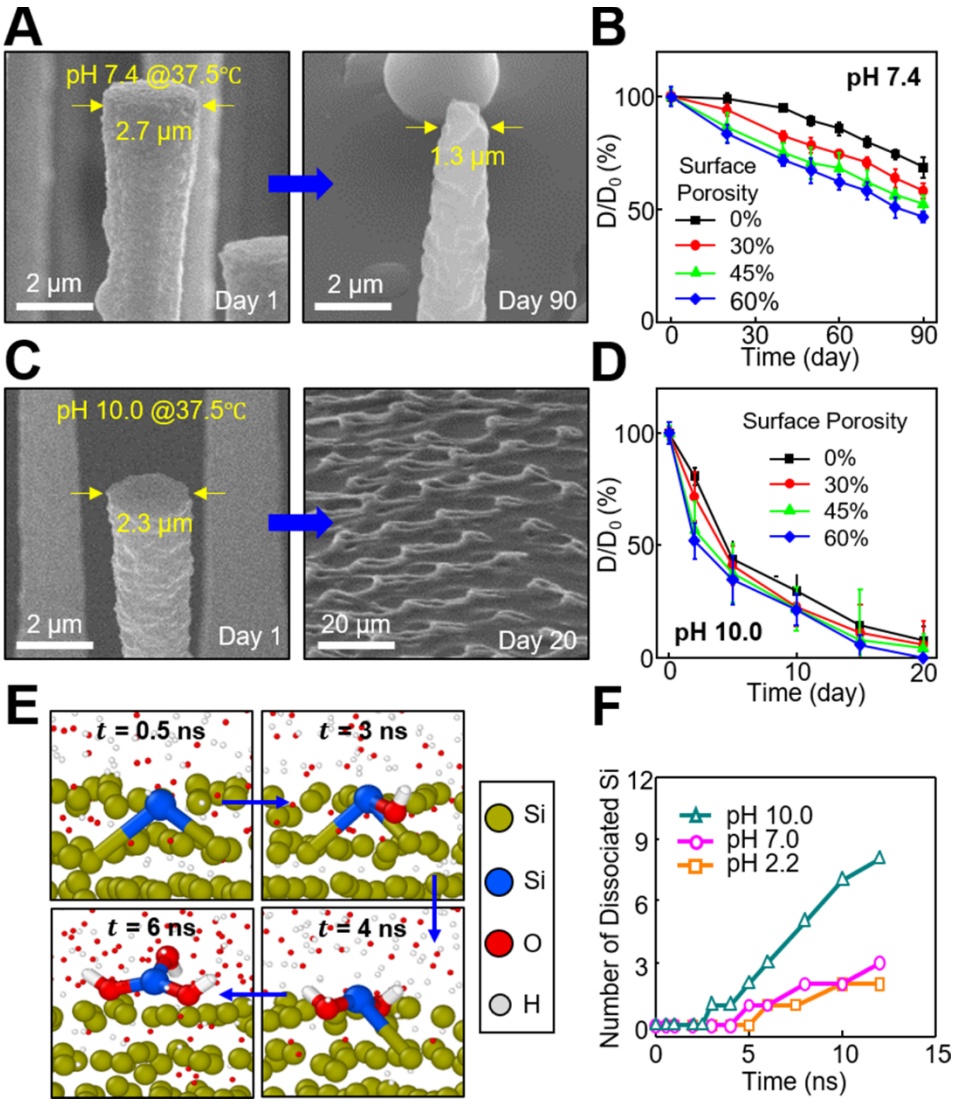

Figure 2. Dissolution of p-Si nanoneedles in biofluids. (A) SEM images of p-Si nanoneedles immersed in 50 ml of PBS (pH 7.4) at 37.5°C for 90 days. (B) Measurement results of D/D_0 ratio (%) obtained from p-Si nanoneedles with varied surface porosities of 0% (black), 30% (red), 45% (green) and 60% (blue). (C) SEM images of p-Si nanoneedles immersed in 50 ml of PBS (pH 10.0) at 37.5°C for 20 days. (D) Measurement results of D/D_0 ratio (%) obtained from p-Si nanoneedles with different surface porosities. (E) Snapshot images of MD simulation at different time frames. (F) Simulation results for the variation of number of dissociated Si atoms in solutions at acidic (pH 2.2) and basic (pH 10.0) conditions formed by addition of H+ and OH- groups, respectively, compared to a neutral condition (pH 7.0).

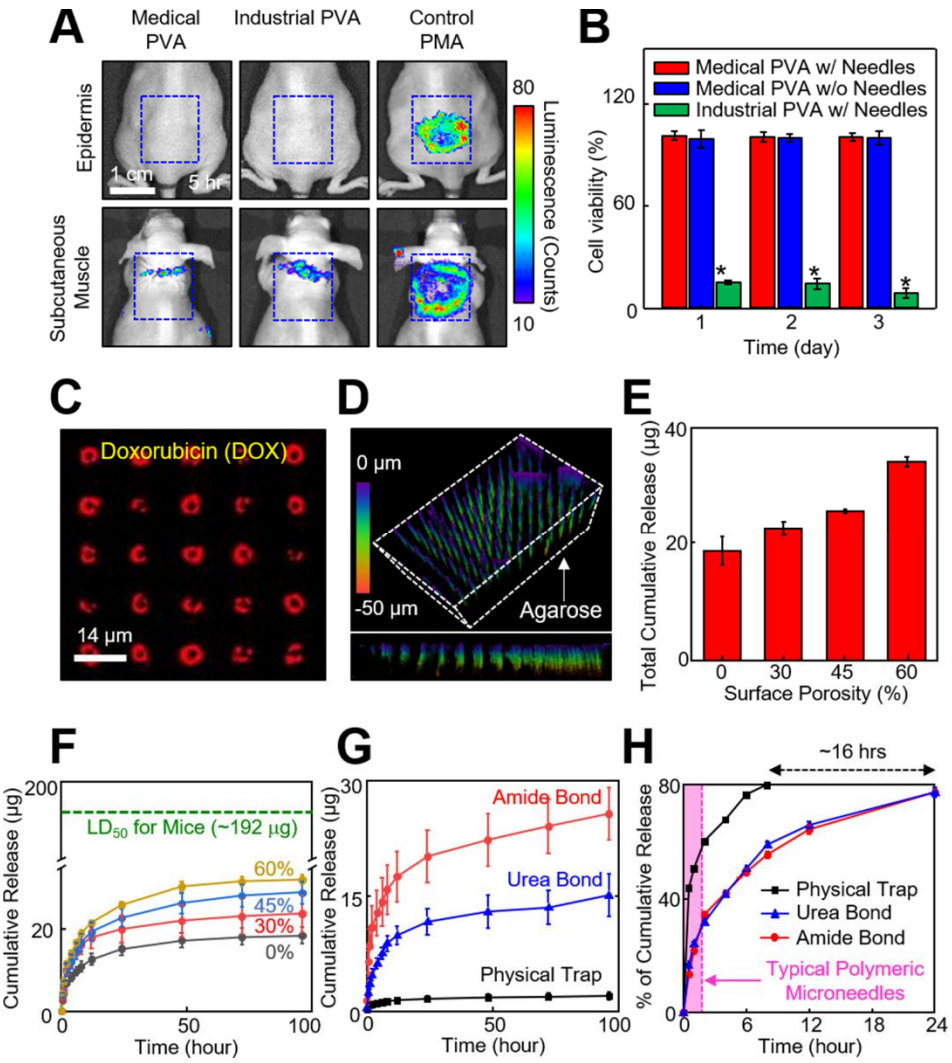

Figure 3. Biocompatibility and controlled drug release. (A) Real-time bioluminescence images on the epidermis (on top of the skin) and subcutaneous muscle (under the skin) of mice at 5 hrs following implementation of medical PVA (left), industrial PVA (middle), and control PMA treatments (right). (B) Results of MTT assay in the cytotoxicity tests of HDF cells incubated with medical PVA with (red bars) and without (blue bars) p-Si nanoneedles, as well as industrial PVA (green bars). Error bars represent the standard deviation (SD) of three replicates. *p<.0001 compared to the medical PVA with p-Si nanoneedles using one-way analysis of variance (ANOVA). (C) Confocal microscopy image of the p-Si nanoneedles loaded with DOX. (D) Confocal microscopy image of the p-Si nanoneedles embedded inside a 2.8% (w/v) agarose gel (color index by penetration length). (E) Cumulative release of DOX obtained from the p-Si nanoneedles with different surface porosities of 0%, 30%, 45% and 60% after 20 days of immersion in PBS (pH 7.4) at 37.5°C. (F) Release profiles obtained from the p-Si nanoneedles with covalently linked DOX, compared to median lethal dose of DOX in mice (LD_{50}, green dotted line). (G) Release profiles obtained from the p-Si nanoneedles (surface porosity = 45%) with DOX by amide bonding (red line), urea bonding (blue line), and control physical trapping (black line). (H) Cumulative release (%) of the covalently linked DOX, compared to the physically trapped DOX.

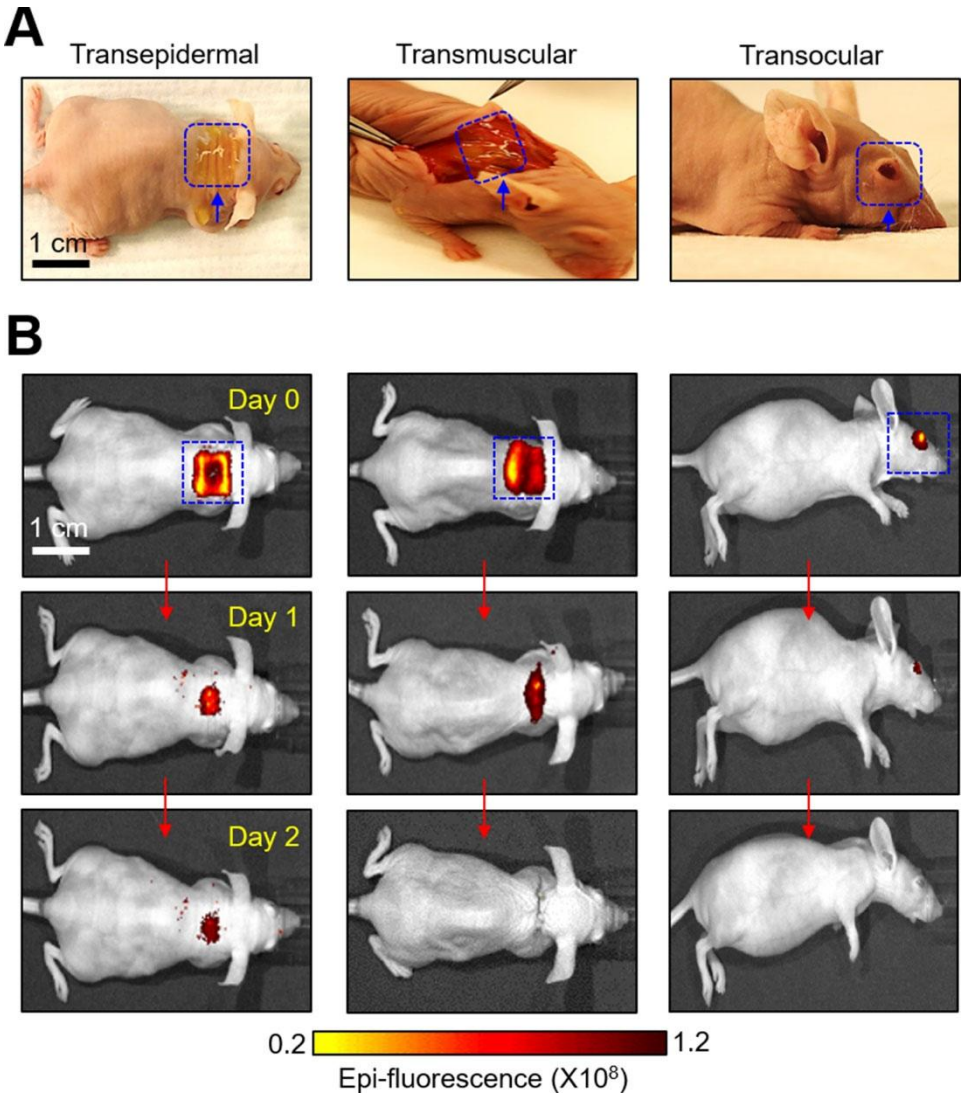

Figure 4. Unobtrusive topical application of p-Si nanoneedles. (A) Optical images of p-Si nanoneedles with DyLight 800 fluorescent dyes on water-soluble backing, each of which, applied to the epidermis, subcutaneous muscle, and cornea of mice. (B) IVIS images of the mice interfaced with the p-Si nanoneedles for 2 days following the implementations.

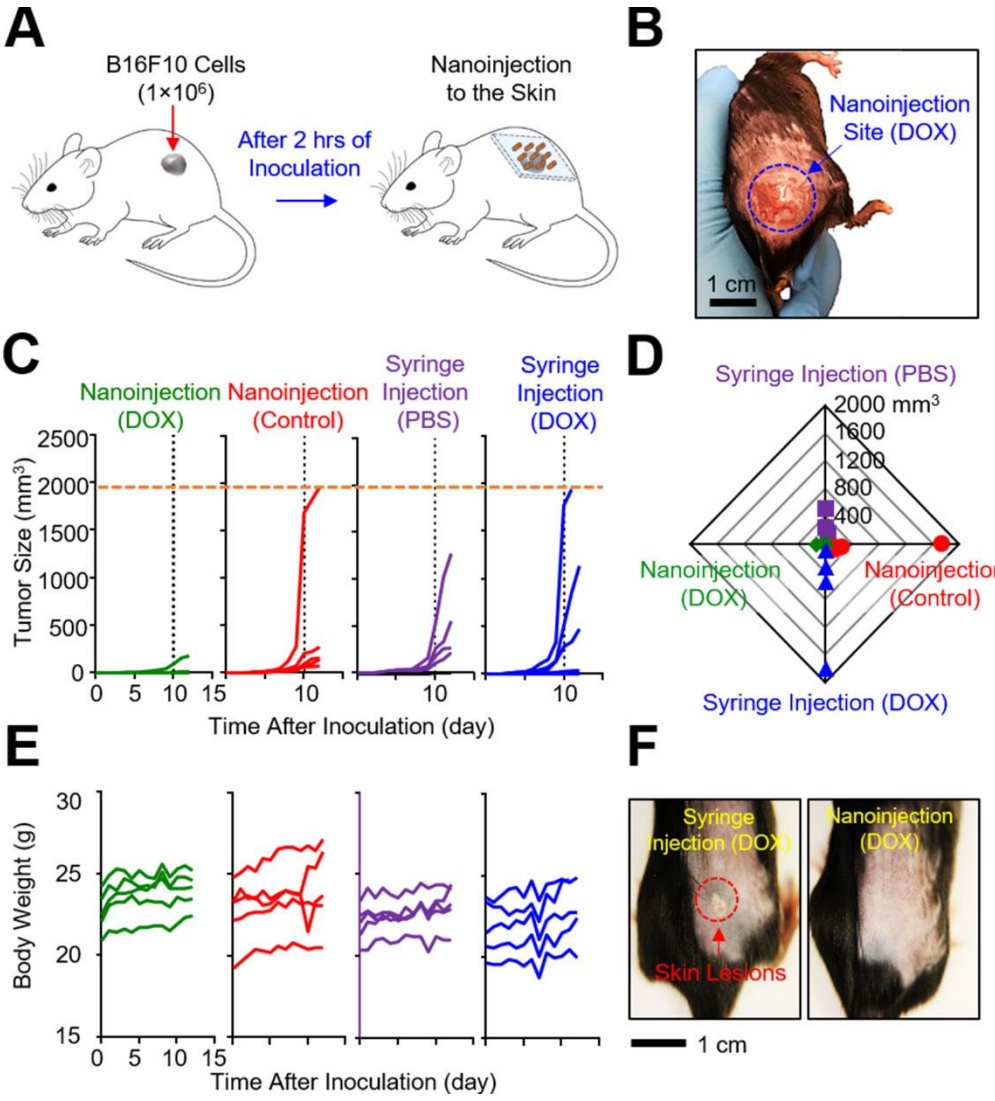

Figure 5. Demonstration on a murine melanoma model in vivo. (A) Schematic illustration of experimental protocols for in vivo studies with a murine melanoma model in mice. (B) Representative image of the shaved skin of a mouse post-nanoinjection of DOX. (C) Measurement results of the tumor size for 12 days post-inoculation (n = 5 per group). (D) Radial shape graph of the tumor size at day 10 (n = 5 per group). (E) Measurement results of the body weight for 12 days post-inoculation (n = 5 per group). (F) Representative images highlighting the treated locations 10 days post-injection. The red dotted circle indicates the skin lesions.

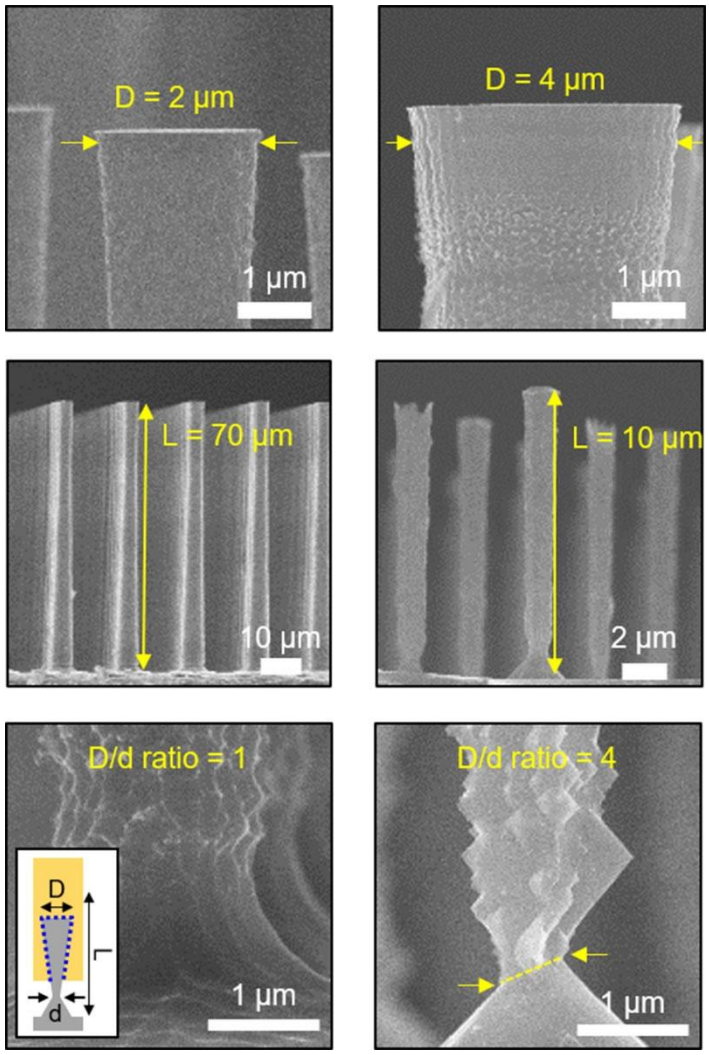

Figure S1. SEM images of p-Si nanoneedles fabricated on a Si wafer with varied sizes. The inset schematic defines the base diameter (D) and undercut diameter (d) of the p-Si nanoneedles.

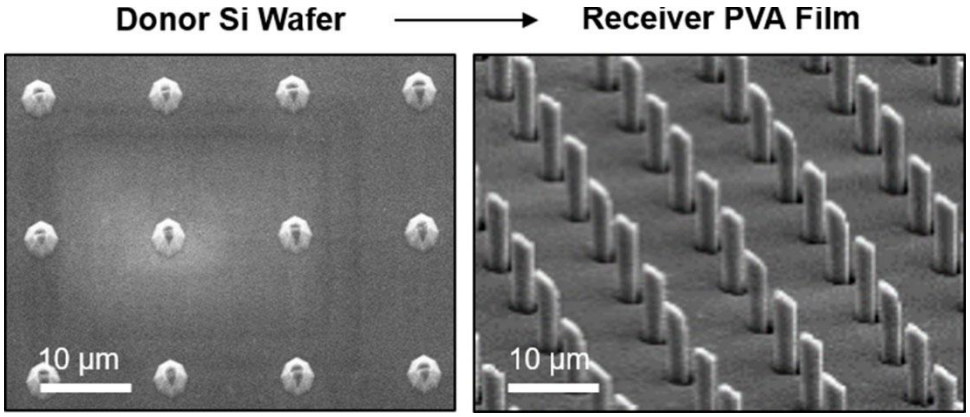

Figure S2. SEM images of representative donor Si wafer (left) and receiver PVA film (right).

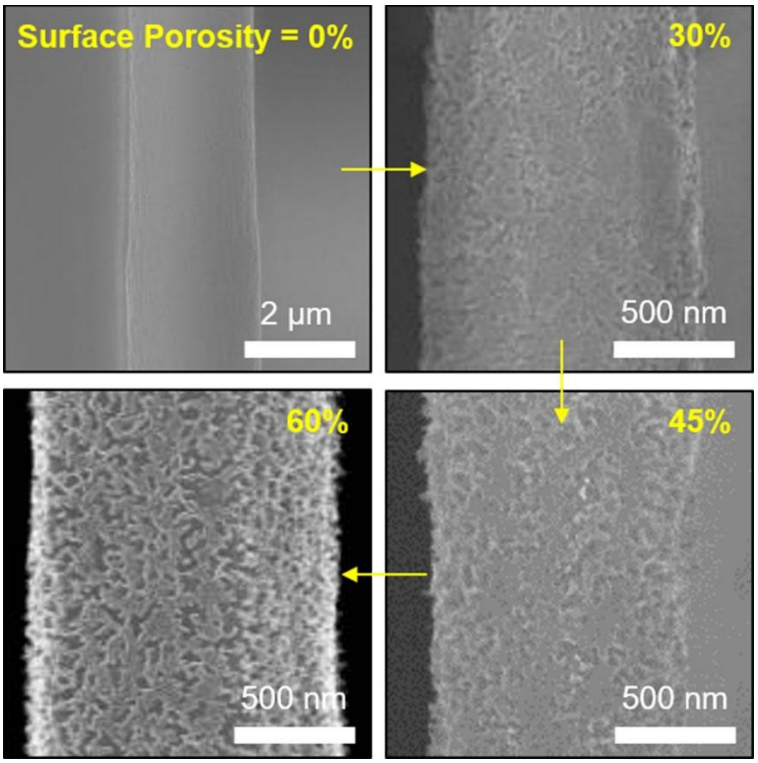

Figure S3. SEM images of p-Si nanoneedles with different surface porosities of 0%, 30%, 45%, and 60%.

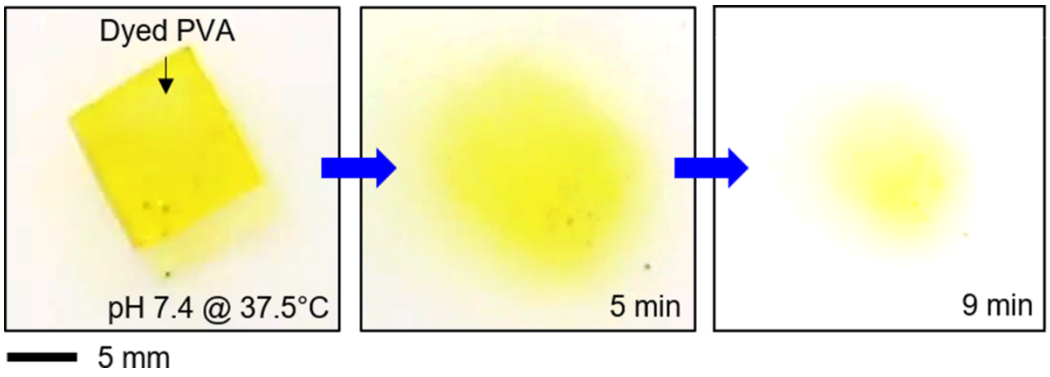

Figure S4. Time-dependent optical images of a yellow-colored PVA film immersed in a solution of PBS (pH 7.4) at 37.5°C.

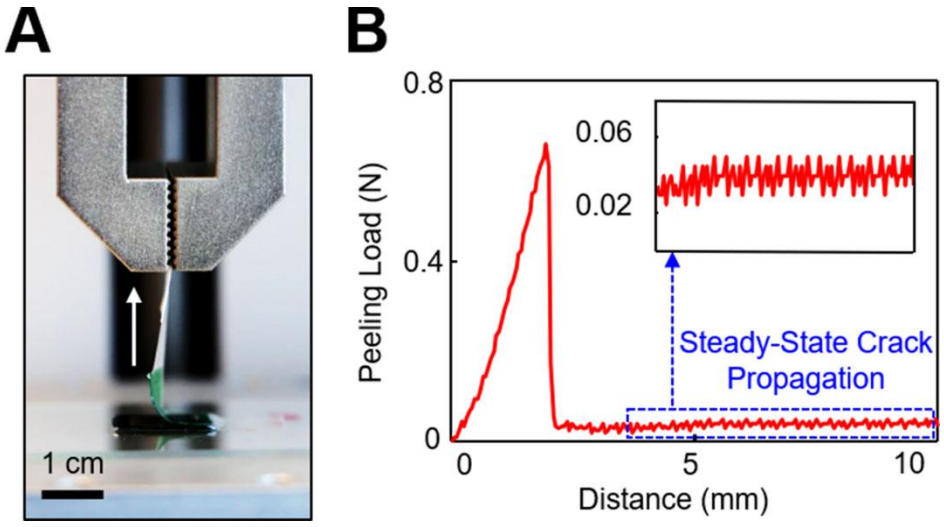

Figure S5. (A) Optical image of an experimental setup for the automated peeling of p-Si nanoneedles from their fabrication Si wafer. (B) Measurement results of peeling load obtained from a unit specimen (1×1 cm^2).

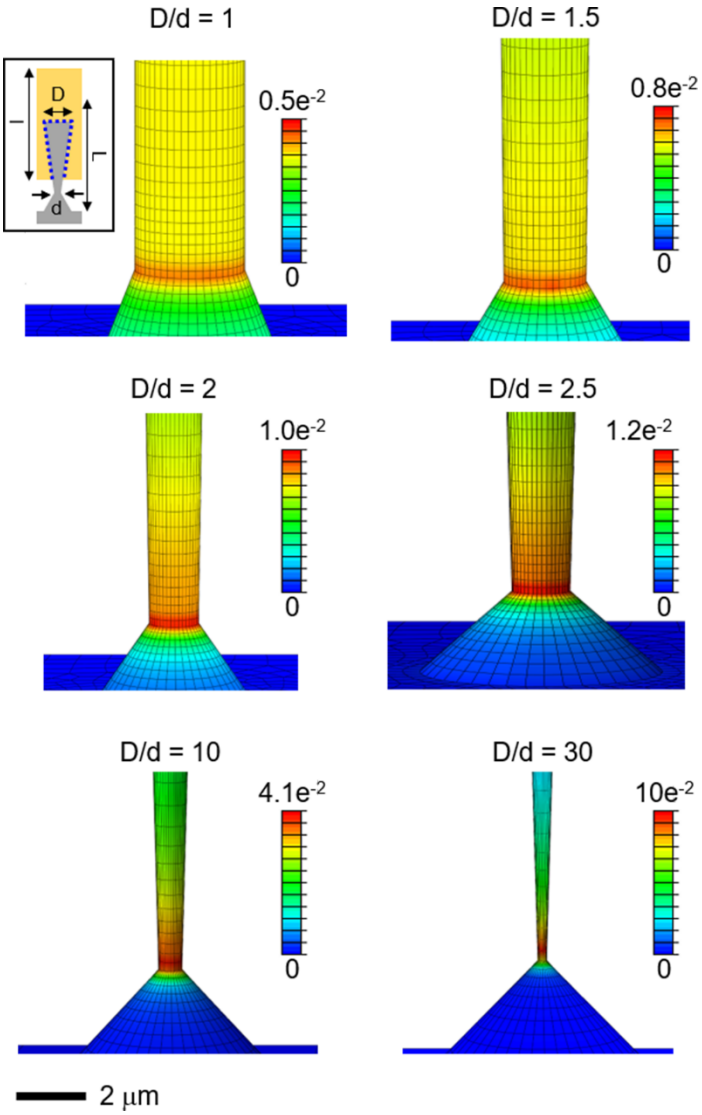

Figure S6. Computational (FEA) results displaying the distribution of principal strains along p-Si nanoneedles with varied D/d ratios under constant mechanical peeling.

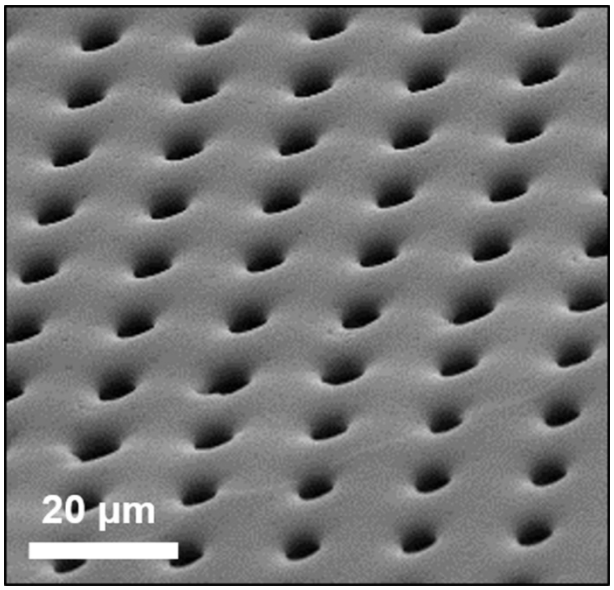

Figure S7. Representative SEM image displaying the compressed marks leftover on the surface of a PVA film peeled out of optimal conditions.

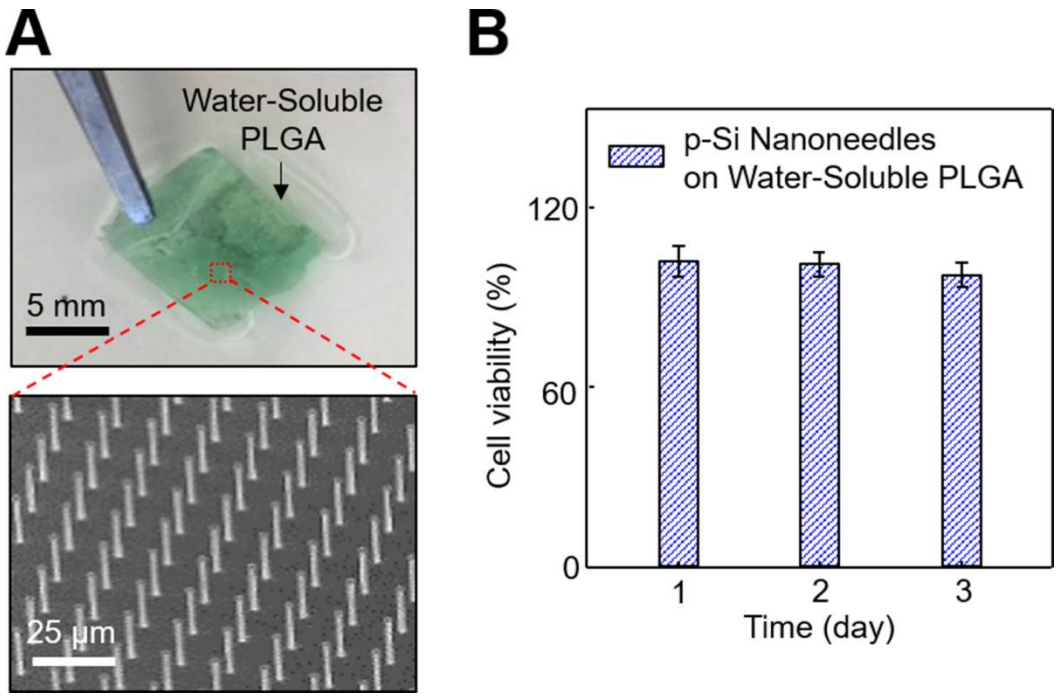

Figure S8. (A) Photo (top) and SEM (Bottom) images of p-Si nanoneedles built on a water-soluble PLGA film. (B) Results of MTT assay in the cytotoxicity tests of HDF cells incubated with the p-Si nanoneedles on the PLGA film. Error bars represent the SD of three replicates.SEM image displaying the compressed marks leftover on the surface of a PVA film peeled out of optimal conditions.

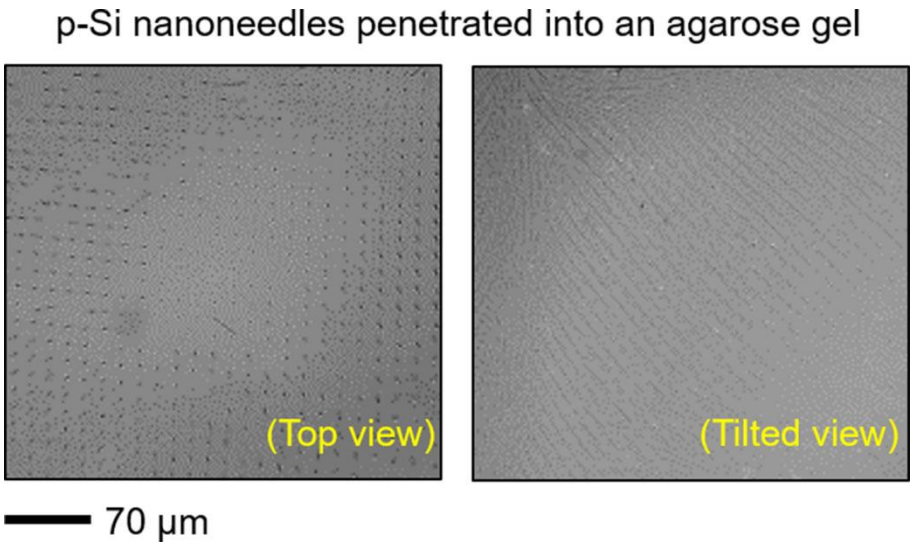

Figure S9. Top-view (left) and tilted-view (right) microscope images of p-Si nanoneedles embedded inside a 2.8% (w/v) agarose gel.

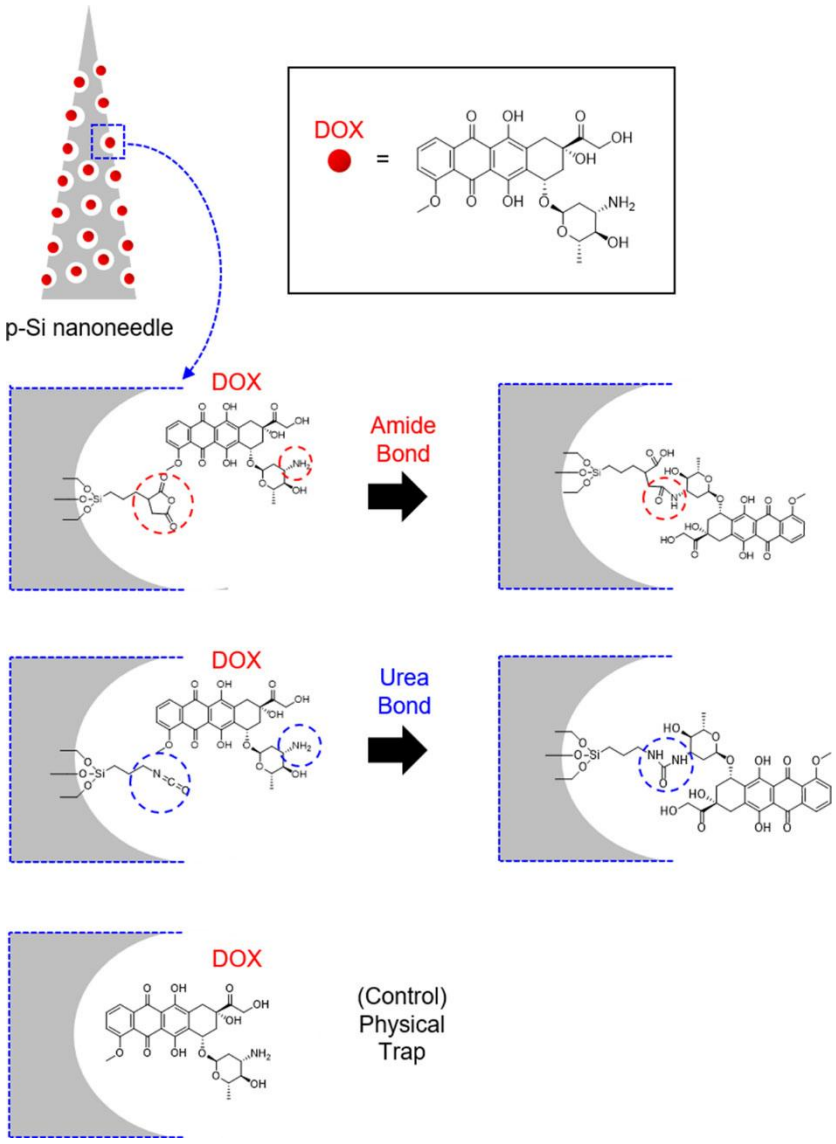

Figure S10. Schematic illustration of amide bonding, urea bonding, and (control) physical trapping of DOX on the surface of a single p-Si nanoneedle.

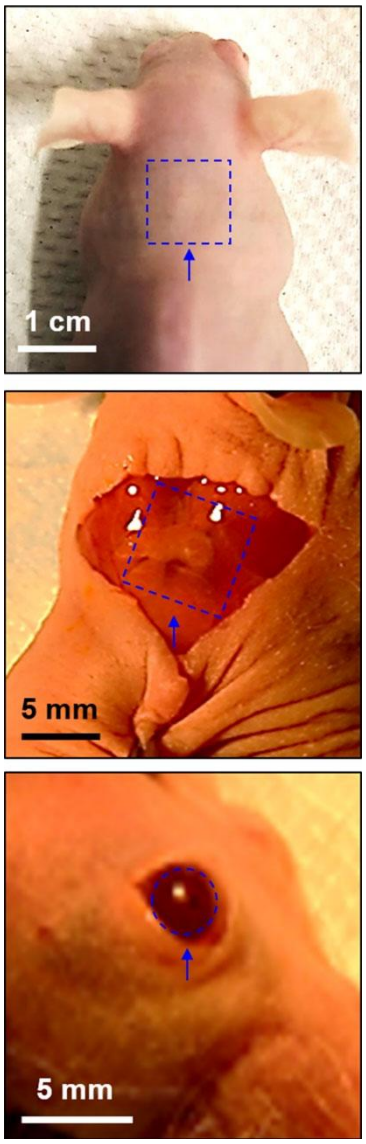

Figure S11. Enlarged optical images of the epidermis, subcutaneous muscle, and cornea of mice receiving an array (1×1 cm^2) of p-Si nanoneedles.

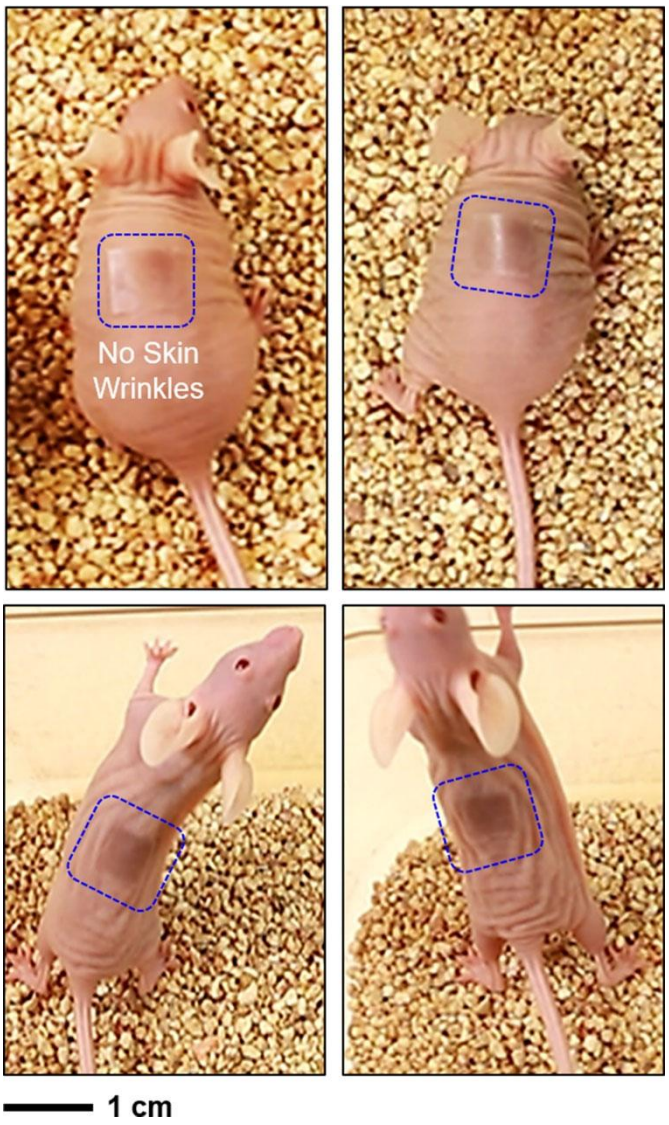

Figure S12. Optical images of (control) p-Si nanoneedles built on a PDMS film and attached on the backside of a nude mouse.

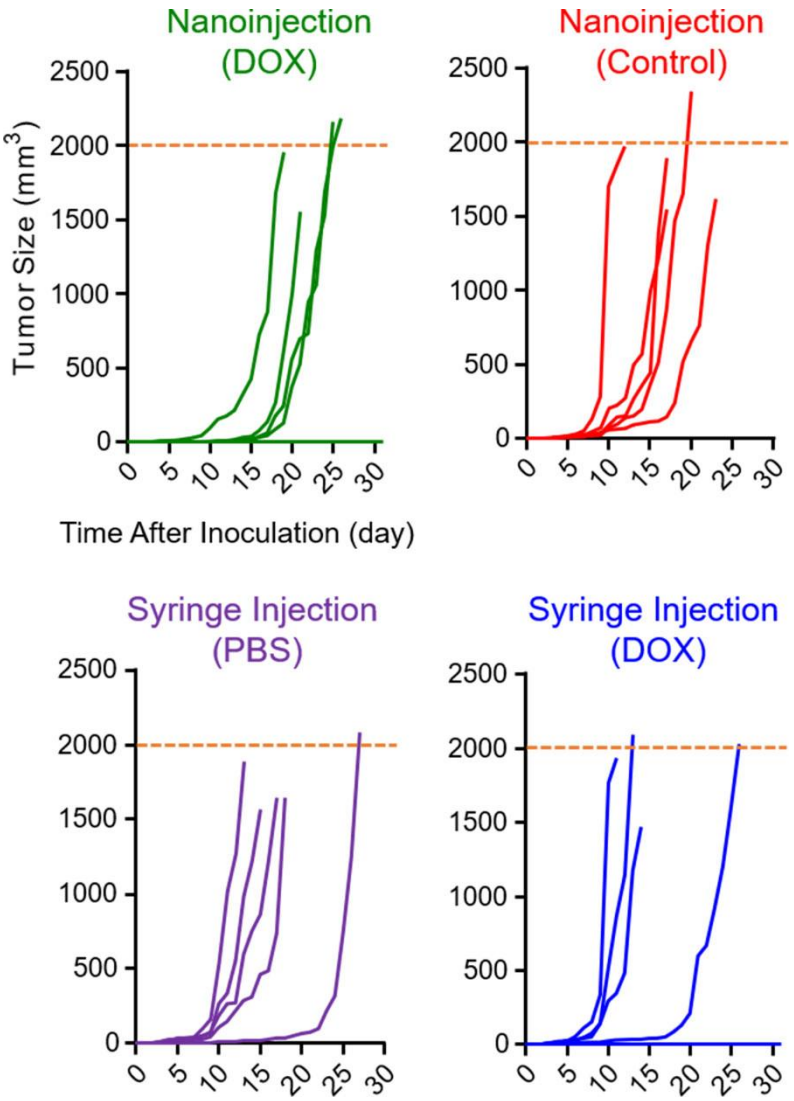

Figure S13. Measurement results for the growth of tumor size (n = 5 per group). The mice were humanely sacrificed when the tumor size reached the endpoint of 2,000 mm^3.

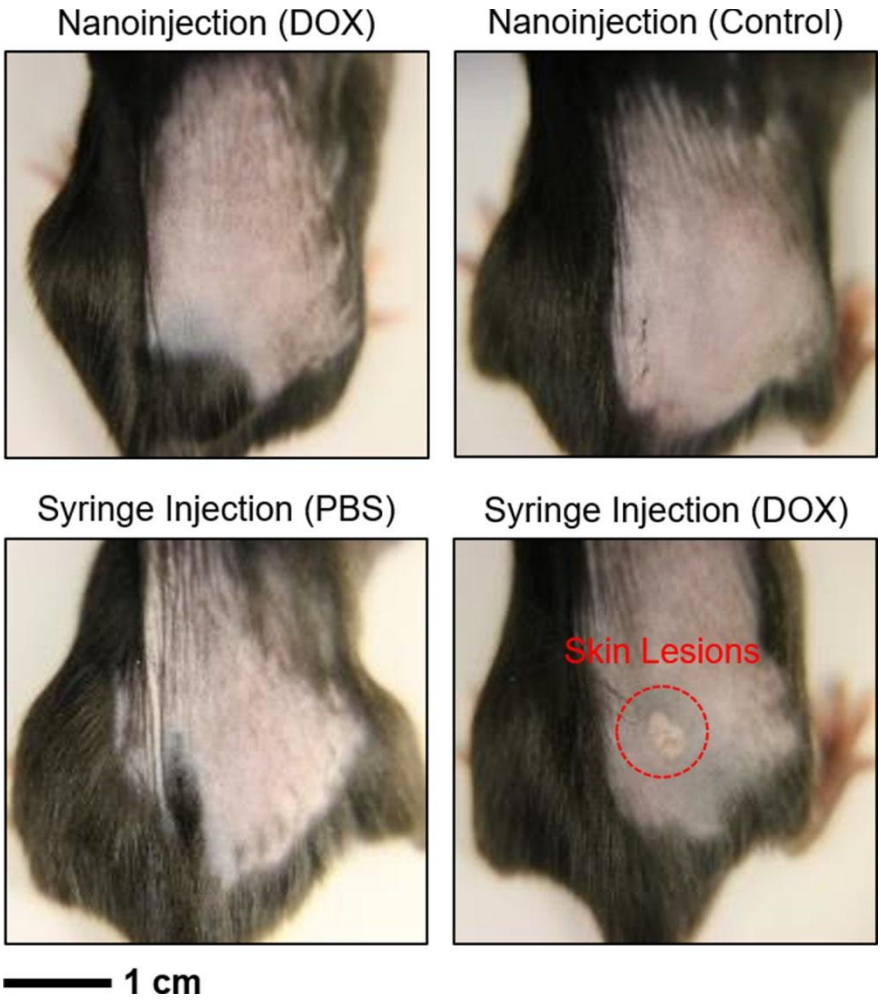

Figure S14. Enlarged optical images of the treated location of the mice at 10 days post-injection.